

1 Motor Cortex Coverage Predicts Signal Strength of a Stentrode Endovascular 2 Brain-Computer Interface

3
4 **Authors:** Hunter R. Schone*^{1,2}, Peter Yoo³, Adam Fry³, Nikole Chetty⁴, Abbey Sawyer⁵,
5 Cara Herbers³, Fang Liu^{1,2}, Chan Hong Moon⁶, Katya Hill⁷, Shahram Majidi⁵,
6 Noam Y. Harel⁵, Raul G. Nogueira⁸, Elad Levy⁹, David F. Putrino⁷, David
7 Lacomis^{8,10}, Thomas J. Oxley^{3,11}, Douglas J. Weber^{4,12}, Jennifer L. Collinger*^{1,2,12}

8
9 ¹Rehab Neural Engineering Labs, University of Pittsburgh, Pittsburgh, PA, USA

10 ²Department of Physical Medicine and Rehabilitation, University of Pittsburgh, Pittsburgh, PA, USA

11 ³Synchron, Inc., New York City, NY, USA

12 ⁴Department of Mechanical Engineering, Carnegie Mellon University, Pittsburgh, PA, USA

13 ⁵Icahn School of Medicine at Mount Sinai Hospital, New York City, NY, USA

14 ⁶Department of Radiology, University of Pittsburgh, Pittsburgh, PA, USA

15 ⁷School of Health and Rehabilitation Sciences, University of Pittsburgh, PA, USA

16 ⁸University of Pittsburgh Medical Center, Pittsburgh, PA, USA

17 ⁹Departments of Neurosurgery and Radiology, University of Buffalo, Buffalo, NY, USA

18 ¹⁰Departments of Neurology and Pathology, University of Pittsburgh School of Medicine,
19 Pittsburgh, PA, USA

20 ¹¹Royal Melbourne Hospital, University of Melbourne, Melbourne, AUS

21 ¹²Department of Bioengineering, University of Pittsburgh, Pittsburgh, PA, USA

22
23 *Corresponding authors: collinger@pitt.edu; schonehunter@gmail.com

24 **Abstract**

25
26
27 Brain-computer interfaces (BCIs) are an emerging assistive technology for individuals with
28 motor impairments, enabling the command of digital devices using neural signals. The
29 Stentrode BCI is an implant, positioned within the brain's neurovasculature, that can record
30 movement-related electrocortical activity. Over 5 years, 10 participants (8 amyotrophic lateral
31 sclerosis, 1 primary lateral sclerosis, 1 brainstem stroke) have been implanted with a Stentrode
32 BCI and significant inter-participant variability has been observed in the recorded motor signal
33 strength. This variability warrants a critical investigation to characterize potential predictors of
34 signal strength to promote more successful BCI control in future participants. Therefore, we
35 investigated the relationship between Stentrode BCI motor signal strength and a variety of user-
36 specific factors: (1) clinical status, (2) pre-implant functional activity, (3) peri-implant
37 neuroanatomy, (4) peri-implant neurovasculature, and (5) Stentrode device integrity. Data from
38 10 implanted participants, including clinical demographics, pre- and post-implant neuroimaging
39 and longitudinal Stentrode BCI motor signal assessments were acquired over a year. Across all
40 potential predictors, the strongest predictor of Stentrode motor signal strength was the degree to
41 which the Stentrode BCI's deployment position overlapped with primary motor cortex (M1).
42 These findings highlight the importance of targeting M1 during device deployment and, more
43 generally, provides a scientific framework for investigating the role of user-specific factors on
44 BCI device outcomes.

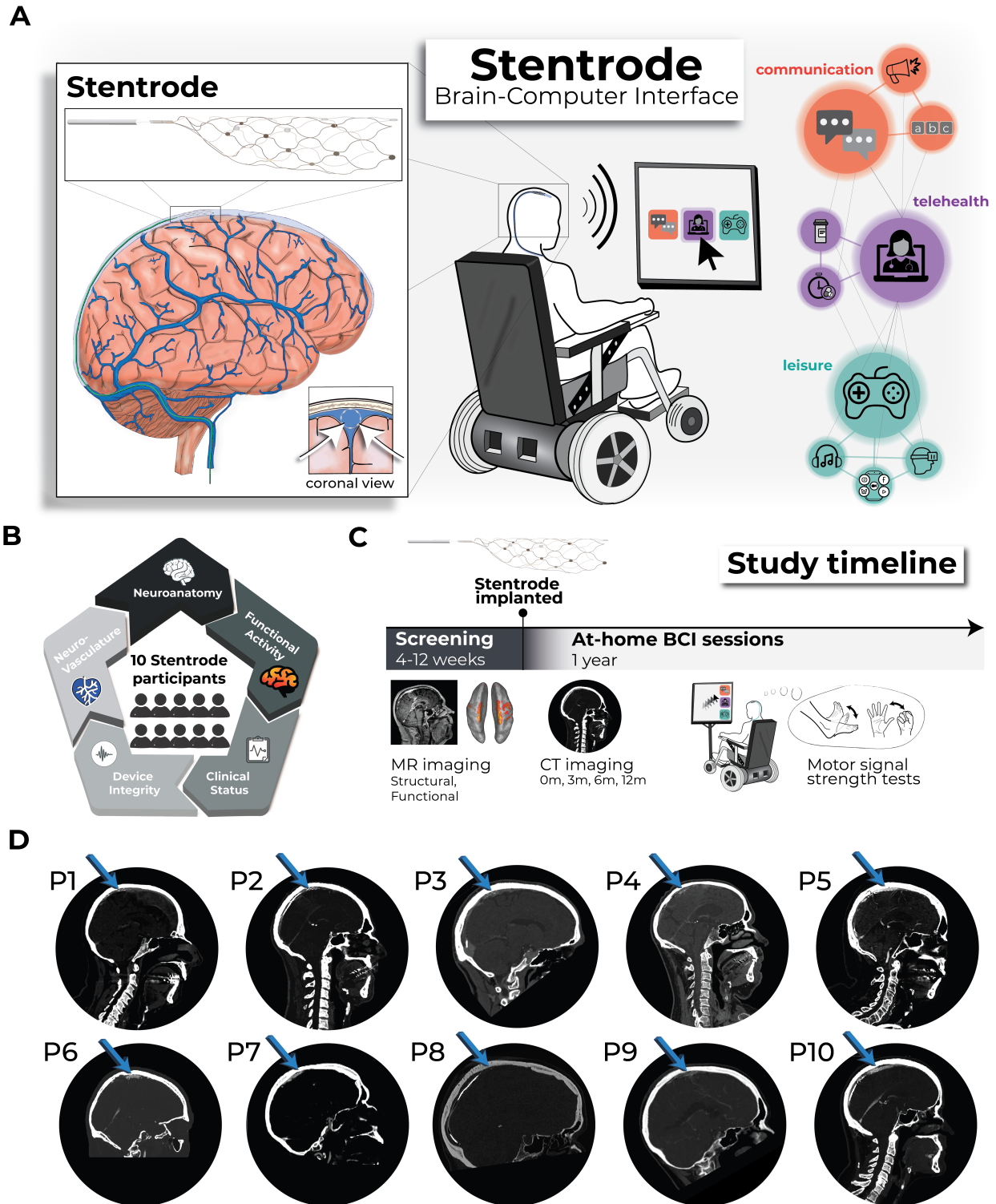
45 Introduction

46
47 Since the first chronic implant in 1998, brain-computer interfaces (BCI) have steadily emerged
48 as an increasingly feasible class of assistive technology¹. Typically designed for individuals with
49 motor impairments (e.g., due to spinal cord injury, stroke, or amyotrophic lateral sclerosis), BCIs
50 translate brain signals into digital commands, circumventing impaired peripheral motor
51 pathways to facilitate control of digital and physical end-effectors (e.g., computer cursors,
52 robotic limbs), enable digital communication, and offer social engagement via online platforms².
53 Existing BCI systems can record brain signals at different locations, with systems using
54 electrodes placed on the surface of the scalp or electrodes that interface directly within brain
55 tissue. Each interface site offers distinct trade-offs in signal fidelity, surgical invasiveness, long-
56 term usability and widespread adoption¹. Scalp electroencephalography BCIs take a
57 noninvasive approach, but suffer from limited signal resolution and prolonged setup times³.
58 Subdural electrocorticography (ECoG) makes use of electrodes laid on the surface of the brain
59 and intracortical microelectrode arrays are inserted directly into the cortical tissue. These
60 techniques offer high-resolution neural recordings, but require a craniotomy, i.e., open-brain
61 surgery, thus limiting widespread adoption. Additionally, electrodes implanted directly into brain
62 tissue exhibit a decline in signal quality over time, due to a biological neuroinflammatory
63 response in the brain⁴ and material degradation^{5–8}. An emerging alternative interface, the
64 Stentrode BCI (developed by *Synchron, USA*), is an endovascular stent-electrode array that is
65 implanted into the brain's vasculature using common endovascular procedures. To date, the
66 Stentrode BCI has been placed in the superior sagittal sinus (SSS), a large vein which lies at
67 the midline of the brain, between the hemispheres of the brain. Unlike subdural ECoG and
68 intracortical devices, the deployment approach does not require a craniotomy. Further, by
69 leveraging the location of the neurovasculature relative to the brain, the Stentrode BCI can
70 record distant neural activity without penetrating the cortical surface and is therefore being
71 investigated as an alternative approach to intracortical devices ([Figure 1A](#)).

72
73 Despite the growing number of BCI technologies, only recently have at-home clinical trials
74 begun to test BCI device usability, marking a critical shift in the focus from proof-of-concept
75 demonstrations in controlled laboratory settings to real-world usability and performance
76 evaluations (for a comprehensive review of all human BCI clinical trials⁹). Industry-led feasibility
77 trials, such as those for the Stentrode BCI [Stentrode clinical trials ([Clinicaltrials.gov](https://clinicaltrials.gov)): AUS
78 (n=4): NCT03834857^{10,11}; USA (n=6): NCT05035823], have investigated the safety of the
79 implanted device and provided an opportunity to gather efficacy data, beginning to define for the
80 field what BCI usability looks like in users' daily lives. However, experience from at-home use of
81 the Stentrode BCI—and similar observations from other BCI technologies—has highlighted a
82 new challenge: BCI signal strength can vary substantially across participants^{12–15}. Moving
83 forward, it is necessary to identify which user-specific factors most reliably predict BCI signal
84 strength for each device, whether related to a participant's clinical status, device design, or
85 where the BCI is implanted. This information is critical for designing pivotal clinical trials that
86 drive the technology's path to widespread clinical use. Further, considering the clinical risks for
87 any BCI implantation procedure and the costs and resources required to implant a single BCI
88 device, it is necessary to critically evaluate, at this stage, whether any user-specific factors can
89 predict the inter-participant variability in Stentrode BCI motor signal strength. Crucially, this
90 question—what factors best predict successful BCI use—extends beyond endovascular BCIs to
91 the entire field, where predicting and optimizing BCI performance is going to be essential for the
92 widespread clinical deployment of devices and selecting the best BCI technology for each
93 patient's neuroanatomy, clinical status and functional needs.

94

95 In the present work, we aimed to identify factors that may contribute to neural signal strength
96 recorded in individuals who had been implanted with a Stentrode device. We hypothesize that
97 several factors will contribute to the inter-participant variability in BCI motor signal strength,
98 which we define as the amount of modulation in neural recordings during attempted
99 movements¹⁴. Some of these user-specific factors are unique to endovascular BCIs and others
100 are more general (Figure 1B). These include **clinical status**, such as time since diagnosis and
101 severity of motor impairment; **pre-implant cortical function**, reflecting the extent to which
102 users can activate motor cortex during attempted movements as measured by functional
103 neuroimaging; **peri-implant neuroanatomy**, encompassing the spatial proximity of the implant
104 to cortical tissue and specific brain regions; **peri-implant neurovasculature**, such as width of
105 the SSS and its relative distance to the cortical surface; and **device integrity**, specifically the
106 number of active recording electrodes (Figure 1C). To address these open questions, across all
107 participants historically implanted with a Stentrode BCI, we pooled datasets including clinical
108 demographics, functional and structural neuroimaging (pre- and post-implant), and longitudinal
109 Stentrode BCI motor signal strength recordings (n=10; Figure 1D). Combined, our investigation
110 aimed to identify the strongest user-specific predictors of Stentrode BCI motor signal strength.
111 Across all tested predictors, the most significant predictor of Stentrode BCI motor signal
112 strength was how much the Stentrode BCI overlapped with motor cortex, demonstrating that
113 successful endovascular BCI use critically depends on targeting primary motor cortex—
114 highlighting the importance of precise neuroanatomical targeting for future clinical deployment.



115
116 **Figure 1. Study overview investigating participants implanted with a Stentrode BCI. (A)**
117 **Left** – Illustration depicting the Stentrode BCI implanted within the superior sagittal sinus.
118 **Middle** – A Stentrode BCI user is depicted generating digital commands with their neural
119 activity. **Right** – Real-world BCI applications include digital communication (orange), telehealth
120 (purple) and leisure (teal). **(B)** Pooling data across 10 participants in the Stentrode BCI clinical

121 *trial, we tested which user-specific factors drive Stentrode BCI signal strength, including:*
122 *neuroanatomy, pre-implant functional MRI activity, clinical condition, device integrity and*
123 *neurovasculature. (C) Clinical trial timeline: pre-implant screening and at-home BCI sessions.*
124 *(D) Post-implant CT scans of each participant at their 3-month timepoint illustrates the relative*
125 *position of the Stentrode BCI location.*

126

127 **Results**

128

129 Our pipeline involved first **extracting the user-specific factors**, then **quantifying Stentrode**
130 **BCI motor signal strength** during attempted movements across multiple sessions, and finally
131 **building predictive models** to test which factors are associated with signal strength.

132

133 **Clinical status:** Heterogeneity in disease state across study participants

134

135 Ten study participants with motor impairment were implanted with a Stentrode BCI. Nine
136 participants were diagnosed with adult-onset motor neuron diseases [8 amyotrophic lateral
137 sclerosis (ALS); 1 primary lateral sclerosis (PLS; P4); mean \pm STD; 4.5 ± 2.8 years since
138 diagnosis at the time of consent], and 1 participant (P8) was diagnosed with an arterial ischemic
139 stroke in the brainstem (13.5 years since diagnosis at time of consent; see participant
140 demographics in [Supp. Table 1](#)). Participants varied in their functional status at the time of
141 implant (for qualitative descriptions of participant's functional status, see [Supp. Table 1](#)). To
142 quantify motor function, participants were graded on their ability to generate muscle contractions
143 of different body-parts: the fingers, wrist, elbow, shoulder, hip, knee, ankle and toes.
144 Participants varied in their manual muscle testing scores (^{16,17}). We hypothesized that the
145 progression of a participant's motor neuron disease pathology or residual motor strength could
146 be potential predictors of Stentrode BCI motor signal strength.

147

148 **Pre-implant functional neuroimaging:** Preserved ability to activate primary motor cortex

149

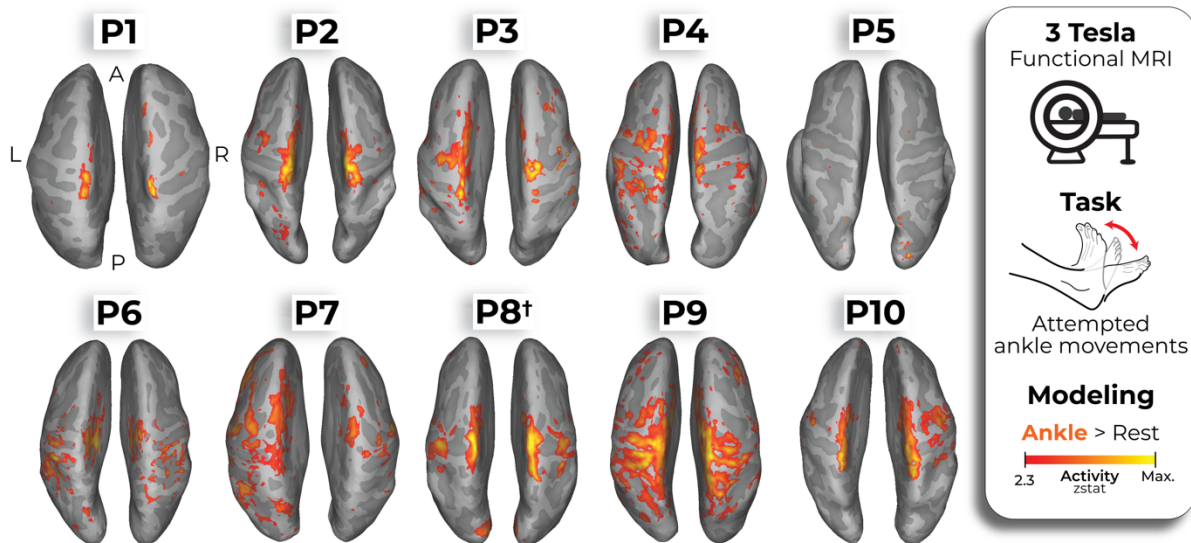
150 Prior to implantation, all participants underwent functional and structural MRI scans (see
151 [Methods](#)). The purpose of the functional MRI was to characterize each participant's ability to
152 functionally activate sensorimotor cortex during attempted movement. Participants needed to
153 show some significant activation of motor cortex in order to be included in the study. During the
154 functional MRI, participants were cued to perform single- or dual-ankle movements. The ankle
155 was selected because ankle cortical activity is highly medial and superior¹⁸, making it the
156 closest representation to the planned Stentrode BCI deployment site within the SSS. Projecting
157 the ankle activation maps for each participant onto the cortical surface revealed widespread
158 activation centered around sensorimotor cortices, though varying in breadth and strength across
159 participants ([Figure 2A](#)). On average, across participants, the majority of the activity was within
160 the boundaries of M1, somatosensory cortex (S1) and the supplementary motor area (SMA;
161 [Figure 2B-C](#)). Further, there were stronger activations in M1 compared to S1 (paired Wilcoxon
162 signed-rank test: $W=47.0$; $p=0.04$) and SMA ($W=49.0$; $p=0.02$). However, the spatial spread of
163 significantly activated voxels ($Z > 2.3$) within each region was largely the same across regions
164 ([Supp. Figure 1A](#); M1 to S1: $W=27.0$; $p=1.0$; M1 to SMA: $W=30$; $p=0.4$; S1 to SMA: $W=35.0$;
165 $p=0.4$).

166

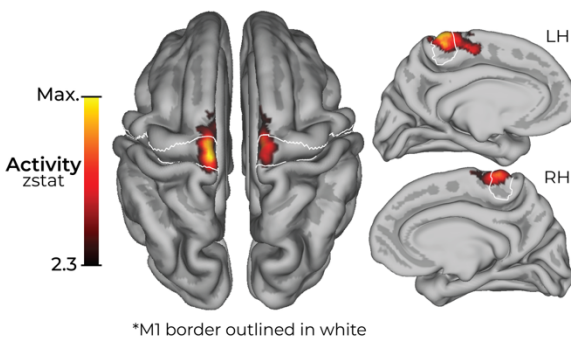
167 We note P5 showed minimal functional activation compared to other participants, though there
168 were still significantly activated voxels for ankle movements (see [Supp. Figure 1A-B](#)). We
169 suspect that the reduced activation volume can be attributed to either poor task compliance
170 during the scan (e.g., poor adherence to the attempted movement or unintended attempted

171 movement during the rest period) and/or due to the late-stage progression of their ALS
172 pathology (11 years since their diagnosis; see the *Discussion* section for more information).
173 However, across all participants we saw no significant relationship between a participant's
174 ability to functionally activate motor cortex (average activation) and years since motor neuron
175 disease diagnosis ($r_s=-0.50$, $p=0.91$). Thus, despite motor neuron disease progression (or P8's
176 brainstem stroke), all participants were able to functionally activate motor cortex during
177 attempted movement. While there is an obvious potential for selection bias given that the ability
178 to activate motor cortex was part of the inclusion criteria, no participants who were screened
179 were excluded for this reason in either clinical trial. However, some did repeat scans to test for
180 significant activation. Aiming to leverage these preserved cortical motor representations to
181 generate digital commands, all participants were then implanted with a Stentrode BCI ([Figure](#)
182 [1D](#); see *Methods*).

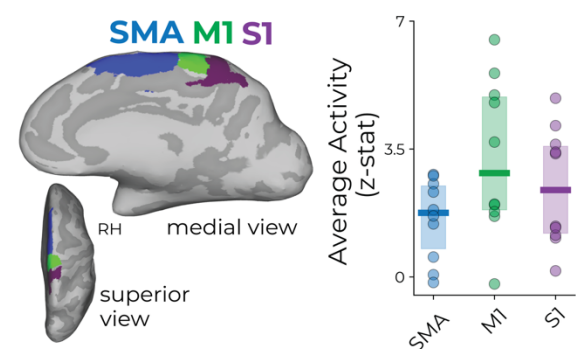
A Ankle functional cortical maps of Stentrode implanted participants



B Group average ankle activity



C Average activity within brain regions

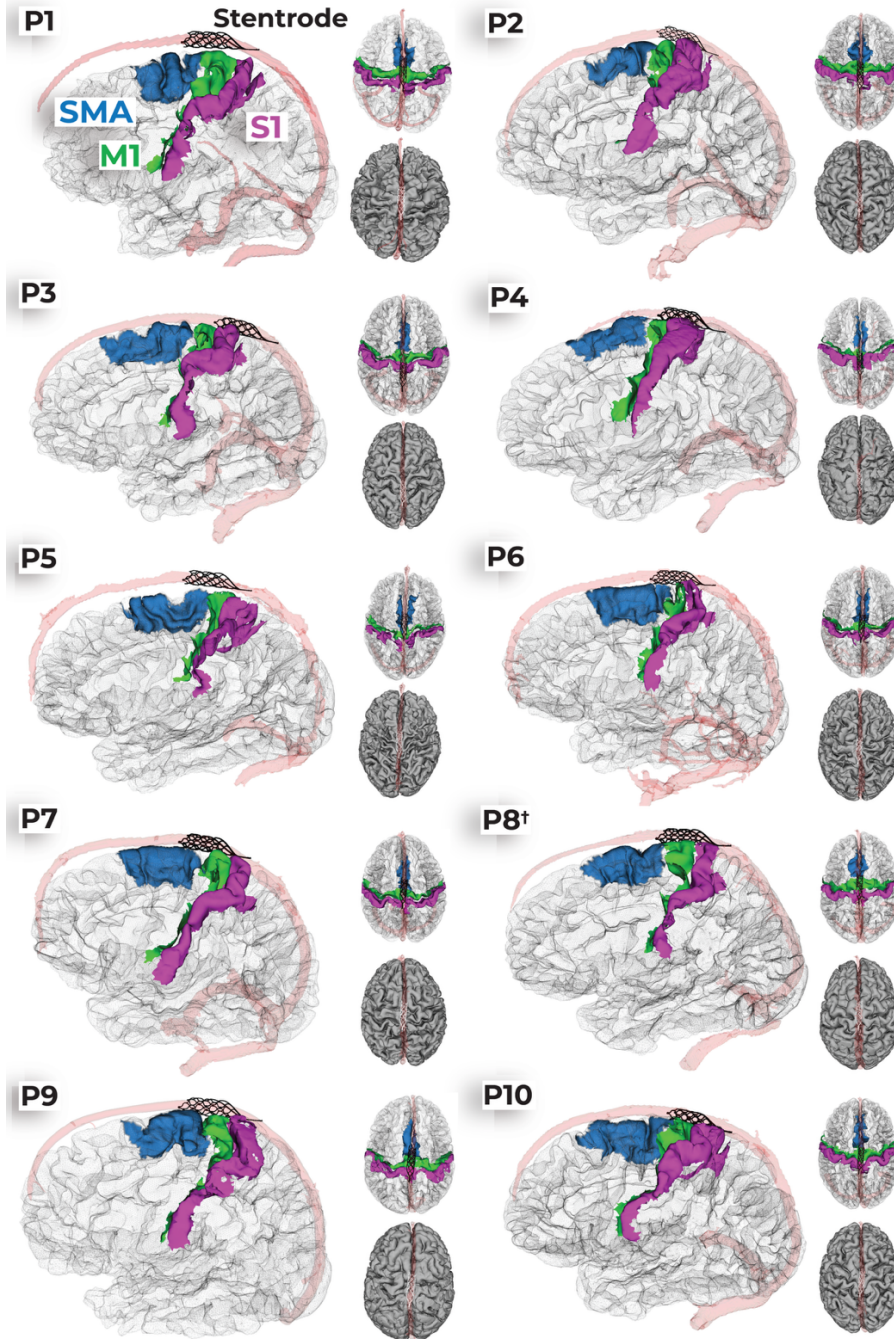


183 **Figure 2. Pre-implant functional neuroimaging of Stentrode-implanted participants. (A)**
184 **Ankle cortical maps of Stentrode-implanted participants.** Using a 3 Tesla MRI scanner,
185 participants were cued to perform ankle movements of either a single ankle or both ankles (see
186 *Methods*). The functional activity for the ankle movement versus rest is projected onto each
187 participant's inflated cortical surface, depicting just the superior view. The activity is minimally
188 thresholded at a z-statistic of 2.3. All participants were diagnosed with adult motor neuron
189 diseases (ALS or PLS), except for P8 who was diagnosed with a pontine arterial ischemic
190 stroke in the brainstem (depicted with a dagger symbol: †). **(B)** Averaging across participants,
191

192 *the group-level average ankle activation map is projected on a standard pial cortical surface.*
193 *The primary motor cortex (M1; BA4) boundary is outlined in white. (C) Performing an ROI-*
194 *specific analysis (averaged across both hemispheres), the M1, S1 and SMA ROIs were reduced*
195 *in size to best capture the relevant ankle activation near the top of the cortical surface, closest*
196 *to the Stentrode BCI deployment site. Left – An example visualization of a participant’s modified*
197 *ROIs shown on an inflated, right hemisphere (RH) cortical surface. Across participants, M1*
198 *exhibited significantly stronger activity than SMA (paired Wilcoxon signed rank test: $W=49.0$,*
199 *$p_{uncorr}=0.02$) and S1 ($W=47.0$, $p_{uncorr}=0.04$). Right – The average activity within each ROI for*
200 *each participant is shown. Blue=SMA; green=M1; purple=S1.*

201 **Structural neuroimaging:** Variability in peri-implant neuroanatomy surrounding the Stentrode
202 BCI

203
204 Next, we used the pre-implant structural MRI to generate high-resolution images of the cortical
205 anatomy and neurovasculature architecture. After participants were implanted with the
206 Stentrode BCI, CT scans were taken to visualize the location of the Stentrode BCI within the
207 superior sagittal sinus (SSS). Each participant's 3-month post-implant CT images ([Figure 1D](#))
208 were registered to their pre-implant structural T1w MRI. This allowed for visualization of each
209 participant's cortical surface reconstruction, neurovasculature and Stentrode BCI segmentations
210 in a common coordinate space ([Figure 3](#); see [Supp. Figure 2](#) for an illustration of the method).
211 Using this aligned data, our goal was to quantify how close the Stentrode BCI was to
212 movement-related neural activity and anatomically-defined cortical regions (i.e., M1, S1, and
213 SMA). We also quantified M1 cortical atrophy for the motor neuron disease participants, since
214 motor neuron disease results in the death of motor neurons as the disease progresses^{19,20}.

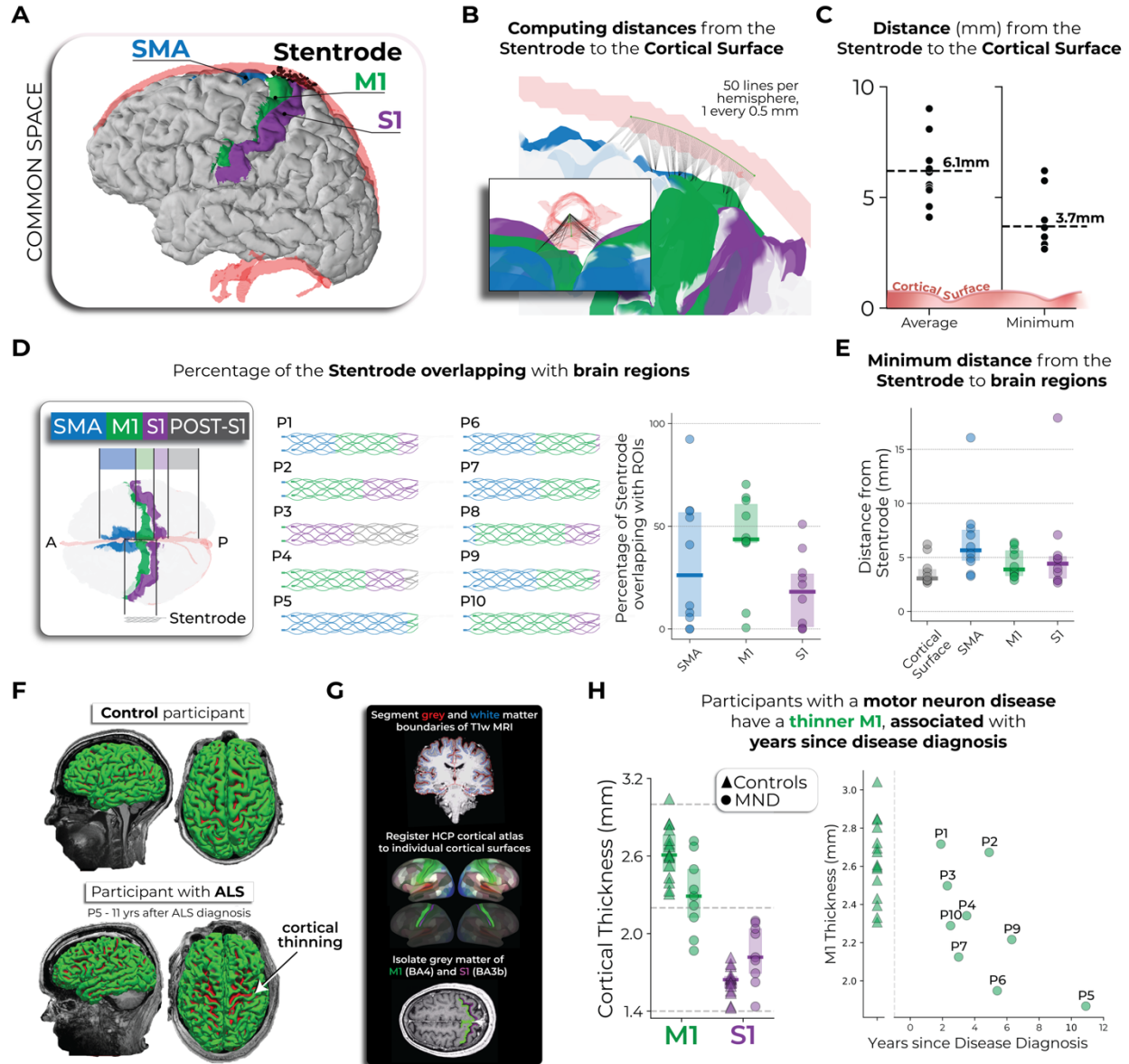


215
216 **Figure 3. Stentrode BCI position for all participants.** For each participant, there are 3 distinct
217 visualizations of the implant position. First, there is a visualization of the sagittal (left) and axial
218 (right top) views of an opaque wire-frame mesh of the cortical surfaces with vertices for specific
219 brain regions colored (supplementary motor area=blue; primary motor cortex=green;
220 somatosensory cortex=pink/purple) and the Stentrode model (black). Second, there is an axial
221 view (right bottom) visualization of each participant's pial cortical surfaces (grey) depicted with
222 both the superior sagittal sinus segmentation (transparent red) and the Stentrode model (white).
223 P8's subject label includes a dagger symbol (†) to reflect their brainstem stroke.
224

225 First, we measured the distance between the Stentrode BCI and the cortical surface. Since
226 individual electrodes are embedded at different points around the circumference of the stent

227 scaffold—some closer to the cortex and others within the opposite wall of the SSS—we created
228 a simplified approximation of its location. Specifically, we generated a 25mm-long line from the
229 most rostral point of the Stentrode CT segmentation, extending caudally, centered within the
230 SSS, and shaped to match its inferior curvature (Figure 4A-B). This approximation was used for
231 all subsequent analyses. To account for cortical folding beneath the vasculature, we calculated
232 (1) the average Stentrode-to-cortex distance across hemispheres and (2) the absolute minimum
233 distance. Across participants, the Stentrode was, on average, 6.1 ± 1.5 mm from the cortical
234 surface, with the minimum distance of $3.7\text{mm} \pm 1.2$ (averaged across participants; Figure 4C).
235 Though, because the array was modelled in the middle of the SSS, the reported values describe
236 the mean electrode-to-cortex separation across the entire Stentrode, rather than the smallest
237 possible clearance of its nearest contact. In addition to measuring distances to cortex, we
238 quantified the width of the SSS vasculature segmentation around the Stentrode implant site,
239 which averaged 7.1 ± 0.9 mm across participants (Supp. Figure 3).

240
241 We next examined the extent to which the Stentrode overlapped with specific brain regions: the
242 SMA (blue), M1 (green), S1 (purple), and any territory caudal to S1 (grey; Figure 4D). While
243 each participant had a unique distribution of overlap across these regions, M1 was the
244 predominant area of coverage for most participants, except for P3 and P5 (for a visualization of
245 all participants cortical surfaces and Stentrode implant position see Figure 3). We repeated the
246 distance calculations shown in Figure 4C for each ROI and found that across participants, the
247 Stentrode was closest to M1 (Figure 4E). Considering this proximity to M1, one important
248 consideration is each participant's disease progression, since motor neuron disease pathology
249 triggers motor neuron death and M1 cortical atrophy^{21–27}. M1 thinning might increase the
250 distance between the Stentrode and desired cortical motor signals, potentially weakening signal
251 strength. For example, see the cortical anatomy of the most progressed participant with ALS in
252 our cohort (P5: 11 years after diagnosis), relative to a control participant without ALS (Figure
253 4F). Data from 16 control participants of a similar age were pooled from a pre-existing dataset²⁸
254 (age of participants with motor neuron diseases vs. control participants: Mann-Whitney
255 independent samples test: $W=109.0$, $p=0.13$). To assess whether cortical thinning was
256 observed among Stentrode-implanted participants with motor neuron diseases, we segmented
257 the grey matter of M1 and S1 for each participant and computed the average thickness of each
258 (Figure 4G). We observed that participants with motor neuron diseases (P8 excluded) exhibited
259 a thinner M1, but not S1, relative to control participants [$n=16$; Figure 4H; rmANOVA: ROI*group
260 interaction: $F_{(1,21)}=19.6$, $p<0.001$; Mann Whitney U tests: M1: $W=101$, $p_{corr}=0.03$; S1: $W=40$,
261 $p_{corr}=0.318$]. Further, M1 thickness was significantly associated with the number of years since
262 their motor neuron disease diagnosis, i.e., participants that were more progressed exhibited a
263 thinner M1 (Spearman correlation: $r_s=-0.70$, $p=0.036$). Further, muscle strength scores were
264 also significantly associated with the cortical thickness of M1 ($r_s=0.76$, $p=0.02$), and not S1
265 ($r_s=0.13$, $p=0.74$), such that participants with less residual muscle strength also exhibited a
266 thinner M1. Combined, the analyses highlight the inter-participant variability in the peri-implant
267 neuroanatomical environment that could potentially contribute to Stentrode signal strength.
268



269
270
271
272
273
274
275
276
277
278
279
280
281
282
283
284

Figure 4. Peri-implant neuroanatomical environment of Stentrode-implemented participants. (A) An example participant's pial cortical surface visualized with their Stentrode segmentation, SSS segmentation, and relevant cortical regions (SMA, M1, S1) registered to the cortical surface. Blue=SMA; green=M1; purple=S1. (B) Approximation of the Stentrode implant position in the SSS and its distance to the cortical surface. Black lines indicate shortest distances to cortex. (C) The average (data on left) and minimum (data on right) distance from the Stentrode line to the cortical surface is displayed. (D-E) Spatial overlap and proximity of each participant's Stentrode with SMA, M1 and S1. (F) Grey matter of a non-ALS control participant (top) and Stentrode-implemented participant with ALS (bottom; 11 years after ALS diagnosis). (G) Method for quantifying cortical thickness. (H) Left – Stentrode-implemented participants with motor neuron diseases (MND; shown as circles) exhibited a thinner M1, not S1, relative to a group of control participants (shown as triangles). Right – M1 cortical thickness was associated with the number of years since each participant's disease diagnosis, i.e., M1 thins with motor neuron disease progression.

285 **Device integrity:** Variability in the number of active recording channels across participants

286

287 The Stentrode BCI has 16 recording channels that are connected to a intravascular lead that
288 runs through the vasculature, from the SSS to the internal jugular vein. Following Stentrode
289 deployment, the lead was inserted into an inductively powered internal telemetry unit (ITU;
290 *Synchron, USA*) positioned in the chest. Due to the difficulty of ensuring a perfect fit, this
291 procedure can lead to some channels having an inactive connection. As such, across
292 participants, the number of active recording channels varies (9 to 16), which could potentially
293 impact Stentrode motor signal strength, particularly if the inactive electrodes were those that
294 would have recorded the most selective movement-related information.

295

296 Due to a technical challenge—and because the participant was the cohort’s only stroke
297 participant, whereas all other participants had ALS or PLS—we excluded P8 from analyses
298 comparing the user-specific factors to Stentrode motor signal strength.

299

300 **Stentrode motor signal strength:** Detecting attempted movement using the Stentrode BCI

301

302 With multiple user-specific factors computed, we next aimed to compute a single measure of
303 Stentrode motor signal strength for each participant. Crucially, we opted to compute a signal
304 strength measure, as opposed to a BCI performance measure due to changes in decoders and
305 electrode referencing across participants and clinical trials. To compute this measure,
306 participants routinely performed motor signal testing (see ref¹⁴), where participants were
307 visually-cued to attempt either hand or foot movements to generate a BCI click within 10
308 seconds, followed by resting (no movement) for 10 seconds (10 repetitions per task run; [Figure](#)
309 [5A](#)). Considering this test was performed within the context of the larger clinical trials and
310 procedures steadily evolved over time, it is worth noting the Motor Signal Test was not
311 administered to all participants in the same manner. These inconsistencies introduce variability
312 in the data collected, including differences in the number of blocks performed per session, total
313 sessions per participant, and the type of imagery strategy attempted (hand or ankle; unilateral or
314 bilateral). Though, to be consistent across participants, we focused on datasets when
315 participant’s used their preferred imagery strategy (n=3 hand-based; n=7 ankle-based; [Supp.](#)
316 [Table 1](#); for data of all imagery strategies see [Supp. Figure 4](#)). For each test block, we isolated
317 the high-gamma frequency band (100 – 200 Hz) across all Stentrode channel recordings and
318 computed a sensitivity index between the density of the burst count during the move epochs
319 versus the rest epochs (see Methods; [Figure 5B](#)). Hereafter, we refer to this sensitivity index
320 measure as Stentrode motor signal strength¹⁴.

321

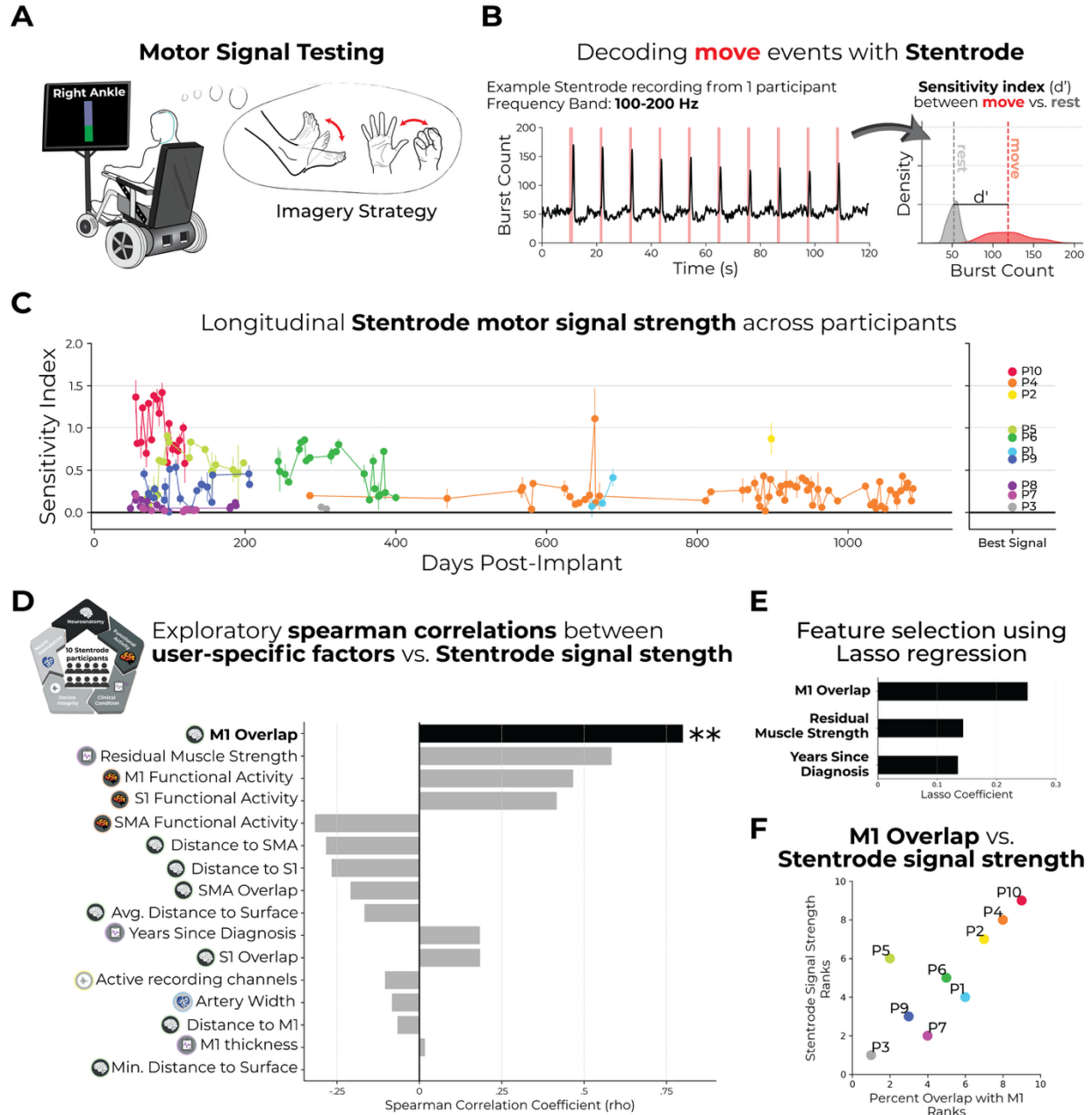
322 For each participant across testing sessions, Stentrode motor signal strength values were
323 significantly greater than 0 (one Wilcoxon signed-rank test per participant; $0.0001 < p < 0.01$; P3
324 was not included in the group analysis due to only having 2 sessions of this task, though both
325 were greater than 0), where a value of 0 reflects no difference in Stentrode recordings during
326 move events and rest events. Across participants and sessions, we observe variability in the
327 magnitude of Stentrode motor signal strength ([Figure 5C](#)). To generate a single value for each
328 participant’s Stentrode motor signal strength to compare to the user-specific factors, we opted to
329 select each participant’s best signal strength value captured in any given test block. The
330 rationale for this decision was to mitigate the inconsistencies in how the task was administered
331 between clinical trials and the progressive nature of motor neuron disease. We note that P4’s
332 best session appears to be an outlier relative to the other sessions ([Figure 5C](#)), however P4 had
333 similarly high values in other sessions when using their non-preferred imagery strategy ([Supp.](#)
334 [Figure 4](#)).

335

336 **Statistical comparisons:** M1 overlap best predicts Stentrode motor signal strength

337

338 Using this measure of Stentrode motor signal strength, we next performed exploratory
339 Spearman correlations to the multiple user-specific factors extracted (16 tests total). Across all
340 tests, we identified only one significant predictor: the percentage of the Stentrode overlapping
341 with M1 ($r_s=0.80$, $p_{uncorr}=0.01$), such that greater M1 overlap reflects increased Stentrode motor
342 signal strength (Figure 5D; for a visualization of all ranked correlations see Supp. Figure 5). To
343 explore the relationships between Stentrode signal strength and the user-specific factors more
344 rigorously, we also performed a feature selection using Lasso regression. This analysis allowed
345 us to identify which factors were most predictive of Stentrode signal strength while penalizing
346 irrelevant or redundant predictors. Among all factors considered, three factors survived, with
347 greater than zero Lasso coefficients: M1 overlap (the highest), followed by residual muscle
348 strength, and years since diagnosis (Figure 5E). Collectively, these tests show the amount of
349 the Stentrode overlapping with motor cortex is the strongest predictor of Stentrode motor signal
350 strength with clinical measures such as residual muscle strength and disease duration
351 contributing additional, complementary explanatory power when considered in combination.
352 (Figure 5F).

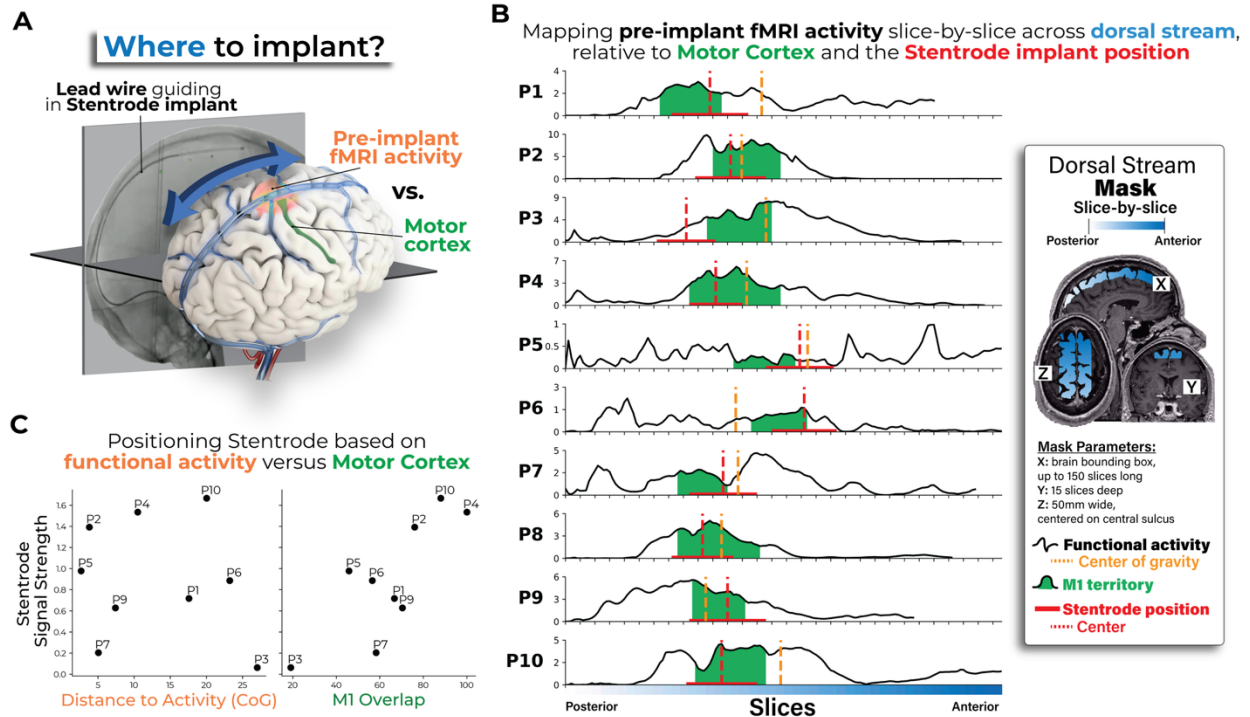


353
 354 **Figure 5. M1 overlap associated with Stentrode BCI motor signal strength.** (A) To quantify
 355 Stentrode BCI signal strength for each participant, participants were visually cued to perform 2
 356 different motor imagery strategies: either an ankle flexion/extension or hand close/open
 357 movement (unilateral or bilateral). (B) **Left** – Example Stentrode BCI recording (100-200 Hz
 358 frequency band) for 1 participant for a single task session. The red line denotes the on/off period
 359 of the movement cue. The black line depicts the Stentrode BCI burst count during the task.
 360 **Right** – A signal sensitivity index (d' -prime) was computed by comparing burst count densities of
 361 ‘rest’ epoched data (shown in grey) versus ‘move’ epoched data (shown in red). (C) **Left** –
 362 Longitudinal Stentrode BCI signal strength (i.e., the sensitivity index) values are shown for all
 363 participants for all testing sessions. The datasets reflect only the blocks where participants used
 364 their preferred imagery strategy. The error bars reflect instances where the task was performed
 365 multiple times in a single session. **Right** – The highest Stentrode BCI signal strength value for a
 366 single session of each participant are plotted. Participants with the highest session signal

367 *strength values are coloured in warm colors and lower in cool colors. (D) When correlating*
368 *Stentrode BCI signal strength to each of the user-specific factors, one significant predictor*
369 *emerged: percentage of the Stentrode BCI overlapping with M1. (E) Similarly, a Lasso*
370 *regression analysis revealed 3 factors with non-zero lasso coefficients: M1 overlap, residual*
371 *muscle strength and years since diagnosis. (F) Visualization of the correlation between the*
372 *percentage of the Stentrode BCI overlapping with M1 and motor signal strength ($r_s=0.80$,*
373 *$p_{uncorr}=0.01$; ranked values shown in correlation).*

374 375 **Considerations for future Stentrode BCI deployment**

376
377 The previous analyses (Figure 5F) show that M1 overlap is associated with Stentrode BCI
378 signal strength. For future Stentrode implant targeting, this result suggests that deployment
379 should specifically target primary motor cortex, defined by its neuroanatomical landmarks, e.g.,
380 the rostral wall of the central sulcus, to maximize Stentrode BCI signal outcomes. However, it is
381 still unclear whether pre-implant fMRI activity can be used to further optimize positioning (Figure
382 6A). To test this, we aimed to directly compare volume-based fMRI activity versus M1 overlap.
383 We performed a volume-based fMRI activity analysis, where we projected the average pre-
384 implant fMRI motor activity for every slice across the dorsal stream, i.e., the cortical surface
385 directly beneath the SSS vasculature. To select the ideal implant location based on the fMRI
386 activity, we computed the center of gravity of this projection. We next identified, for each
387 participant, the slices that overlap with their Stentrode BCI and the M1 brain region. Finally, we
388 computed the distance between the ideal fMRI slice (i.e., center of gravity of movement-related
389 activity) and the slice at the midpoint of where the Stentrode BCI was implanted (Figure 6B).
390 Often the centroid of activity was rostral to the midpoint of the Stentrode. For five out of ten
391 participants, the centroid of activity was within M1; for four participants the centroid was rostral
392 to M1 and for one participant it was caudal to M1. We also computed the percentage of slices
393 that encompassed the Stentrode BCI that overlapped with M1 (Figure 6B). Similar to the
394 surface-based analysis, we observed that M1 overlap, defined on the volume vs. on the surface,
395 also showed a significant association with Stentrode BCI signal strength (Spearman correlation:
396 $r_s=0.70$, $p=0.043$). Alternatively, there was no meaningful relationship between Stentrode signal
397 strength and how far away the Stentrode BCI was from the location of peak fMRI activity ($r_s=-$
398 0.18 , $p=0.64$; Figure 6C). Combined, with the previous analyses, this confirms future Stentrode
399 BCI deployment should prioritize maximizing motor cortex coverage and the present functional
400 MR imaging protocol may be insufficient for improving targeting.



401 **Figure 6. Motor cortex coverage, over functional activity, is strongly associated with**
402 **Stentrode BCI signal strength. (A)** An important consideration when deploying the Stentrode
403 **BCI via a lead wire is deciding where to position the device within the superior sagittal sinus.**
404 **There are two factors to base this decision on: (1) pre-implant fMRI activity, relying on the**
405 **location of the largest cluster of activity or (2) neuroanatomical landmarks, i.e., motor cortex on**
406 **the rostral wall of the central sulcus. (B)** To test which factor impacted signal strength in the
407 **participants, we performed a volume-based analysis. For each participant (each row), we**
408 **projected the average pre-implant fMRI motor activity (black line) for each slice across the**
409 **dorsal stream (white-to-blue colored mask). We then computed the center of gravity of this**
410 **projection across the dorsal stream, depicted as a yellow dashed vertical line. This would reflect**
411 **the best implant site if based solely on the fMRI activity. We next defined the slices that overlap**
412 **with the M1 cortical region (colored in green) and the slices that overlap with the Stentrode BCI**
413 **(red horizontal line; the center point depicted as a red dashed vertical line). (C)** Finally, for each
414 **participant, we then computed (1) the distance between the fMRI center of gravity slice to the**
415 **Stentrode BCI center slice and (2) the percentage of Stentrode slices overlapping with M1**
416 **slices, i.e., M1 coverage. We observed that M1 coverage showed a significant association with**
417 **Stentrode signal strength (Spearman correlation $r_s=0.70$, $p=0.043$). Alternatively, there was no**
418 **meaningful relationship with the distance to the ideal fMRI slice and Stentrode BCI signal**
419 **strength ($r_s=-0.18$, $p=0.64$).**
420

421 Discussion

422
423 Across 10 participants implanted with a Stentrode BCI, we explored the relationship between a
424 variety of user-specific factors and Stentrode BCI motor signal strength. Regardless of
425 impairment level or diagnosis (ALS, PLS or brainstem stroke), participants were able to
426 functionally activate cortical motor networks during attempted movement prior to implantation,
427 confirming that the ability to voluntarily produce cortical motor signals were preserved in the
428 cohort, at least to some degree. Structurally, we observed that the study participants with motor
429 neuron diseases exhibited motor cortical atrophy relative to controls, with cortical thickness
430 correlating with both participants' residual muscle strength and time since disease diagnosis.
431 Additionally, we quantified the inter-participant variability of the peri-implant neural environment
432 across all participants implanted with a Stentrode BCI, relative to specific cortical regions and
433 the neurovasculature. Most importantly, across all tested user-specific factors, we identified that
434 the strongest predictor of BCI motor signal strength was the degree to which the Stentrode
435 implant overlapped with primary motor cortex (M1), emphasizing the importance of precisely
436 targeting M1 during device deployment. Our findings have three main implications for clinical
437 neuroscience research and the development of BCI technologies. Specifically, it (1) highlights
438 the unique neural and clinical considerations for BCI signal strength for individuals living with
439 adult-onset motor neuron diseases, (2) informs the future targeting strategy for Stentrode BCI
440 deployment (and other future BCIs that may use an endovascular electrode deployment
441 approach) and, (3) offers a general investigational framework for testing the impact of user-
442 specific factors on signal strength of BCI technologies.

443
444 First, our results offer a high-level characterization of the neural and clinical factors that need to
445 be considered for successful BCI usability in individuals living with adult-onset motor neuron
446 diseases, a primary target clinical population for BCI technologies. Most common in our cohort,
447 ALS is a heterogenous neurodegenerative disease, marked by progressive motor decline and
448 generally poor prognosis; population studies report a median survival of ~3 years from symptom
449 onset in unventilated cohorts²⁹, but survival can extend well beyond this in individuals who opt
450 for long-term mechanical ventilation or present with slower-progressing variants, such as the
451 flail-arm phenotype that characterized many participants in the present cohort. For people with
452 ALS to successfully use a Stentrode BCI—or any BCI—it is essential they have some intact
453 structure and function of cortical motor networks, with M1 being the dominant region of interest.
454 However, decades of research has investigated how ALS pathology uniquely degrades M1
455 micro- and macro-structure and functioning. ALS pathology most commonly first targets lower
456 motor neurons, followed by pathological changes throughout cortex, particularly a degradation
457 of the upper motor neurons in M1^{19,20,30}. Though, the symptomatic presentation of ALS is highly
458 heterogeneous. Indeed, M1 is the key hub for voluntary motor command output, and multiple
459 studies have demonstrated its vulnerability in later stages of ALS. For example, post-mortem
460 and high-field neuroimaging studies have highlighted that individual's with late-stage ALS exhibit
461 multiple pathologies to M1 micro- cortical structure, including the degeneration of Betz
462 pyramidal cells in layer V³⁰, the accumulation of iron in deeper cortical layers^{19,23}, increased
463 intracellular calcium³¹, and progressive, widespread demyelination, particularly at the
464 boundaries between somatotopic regions¹⁹. In terms of M1 macrostructure, similar to our
465 findings, several cross-sectional studies have demonstrated that individuals with ALS exhibit
466 dramatic cortical atrophy of the precentral gyrus (i.e., pre- and primary-motor cortex), compared
467 to individuals without ALS²¹⁻²⁷. For example, in a recent report of a long-term ECoG BCI case
468 study, longitudinal CT imaging data from 1 participant revealed significant fronto-temporal
469 cortical tissue atrophy over an 8-year period³². Notably, for our investigation, neither M1 cortical
470 atrophy nor the minimum distance between the Stentrode and motor cortex were significant
471 predictors of Stentrode BCI motor signal strength (Figure 5D). Instead, the significant

472 association we observed was with the percentage of the Stentrode BCI overlapping with M1—a
473 distance measure solely on the coronal plane—suggesting that larger Stentrode BCI motor signal
474 strength may be attributed to the maximum number of Stentrode electrodes being closest to
475 motor cortex versus other cortical regions. Indeed, even though the motor cortex progressively
476 atrophies with disease progression, any space between motor cortex and the vasculature is
477 filled with an expanding gap of cerebrospinal fluid (CSF; [Supp. Figure 3](#)). Our results suggest
478 that so long as the overlap with M1 is sufficient, the high electrical signal conductivity of
479 cerebrospinal fluid³³ may still effectively be delivering a selective motor signal to the Stentrode
480 BCI electrodes. This would suggest that cortical atrophy alone should not be an exclusion
481 criteria for Stentrode BCI usability, especially given prior BCI studies demonstrating successful
482 motor decoding in individuals with ALS^{14,32,34–37}.

483
484 Next, looking to M1 cortical function, neuroimaging studies have reported mixed findings on
485 whether individuals with ALS—particularly those who are locked-in—can volitionally activate M1
486 during attempted movements similar to control participants (see ref.³⁸ for a comprehensive
487 review of task-based neuroimaging studies of ALS). While some studies, including a recent
488 high-field neuroimaging case report, observed preserved M1 activity during motor tasks³⁹,
489 others have shown highly variable or diminished responses, likely reflecting the extreme
490 heterogeneity of ALS³⁸. This preservation in cortical motor activity, at least to some degree,
491 could be explained by evidence that people with late-stage ALS show a considerable amount of
492 preservation of the upper motor neurons of M1 output layer V^{40–42}, at least sufficient for
493 generating a motor output signal. However, it remains an open question whether the presence
494 or strength of M1 activity pre-implant can be used as a reliable predictor of BCI performance.
495 The intricate relationship between M1 structure and function and clinical status—including
496 disease duration and residual muscle strength—likely contributes to BCI signal strength. While
497 no single clinical measure was individually significant in explaining variability, both residual
498 muscle strength and years since diagnosis were retained as predictors in the Lasso regression
499 model. This suggests that, although their individual effects may be subtle, these clinical factors
500 may contribute meaningful, non-redundant information when considered alongside the implant’s
501 proximity to M1. These findings underscore that successful BCI use in people with ALS is not
502 determined by any single clinical or neural factor, but instead reflects a complex interplay
503 between disease progression, preserved cortical function, and precise anatomical targeting—
504 highlighting the need for multimodal, individualized assessment in guiding future BCI
505 deployment.

506
507 The most practical implication of our results is they provide immediate guidance on future
508 endovascular BCI deployment strategies, specifically to what degree functional neuroimaging
509 data should be relied on as a targeting guide versus neuroanatomical landmarks (e.g., M1
510 located on the rostral wall of the central sulcus). For both surface- and volume-based analyses,
511 Stentrode BCI overlap with M1 emerged as a predictor of Stentrode BCI motor signal strength.
512 Further, across participants, the spatial landscape of pre-implant functional activity during
513 attempted movement often lacked a clear unimodal structure along the coronal plane, with the
514 largest peak appearing in different regions (i.e., S1, M1 or SMA) at the individual participant
515 level ([Figure 6](#)). In order for personalized functional neuroimaging to be a useful targeting guide,
516 spatially selective functional activations are essential to identify an optimal deployment site.
517 However, in order to visualize more spatially selective activations, it requires changing the MR
518 imaging protocol to incorporate (1) more functional data (e.g., more than the 1-2 runs per
519 participant collected in the present study), and (2) more movement conditions to control for
520 regions responsive to general motor responses, the presence of visual/auditory stimuli during
521 the active epochs, and attentional/motivational drivers of activity. While there is a simple
522 solution, increasing scan times for people with motor neuron diseases, particularly those in

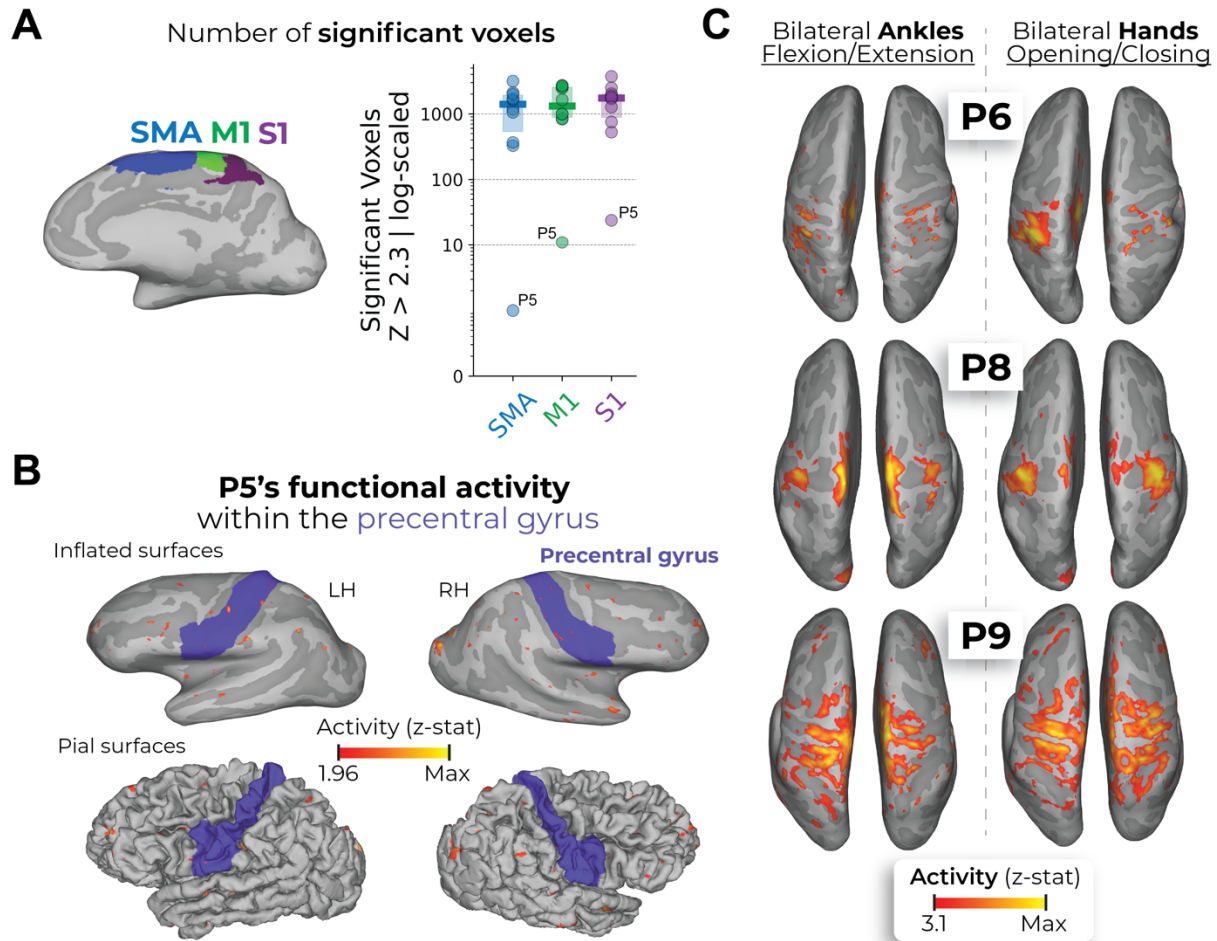
523 advanced stages, has considerable tradeoffs. For example, in the present cohort, 3 participants
524 were mechanically ventilated via a tracheostomy and had minimal to no residual volitional
525 movement of a single body-part (see [Supp. Table 1](#) for descriptions of each participants' clinical
526 state). Scanning these participants required participants being moved off their personal
527 ventilators, manually ventilated by a respiratory therapist and then placed on an MR-compatible
528 ventilator for the duration of the scanning, regularly monitored by a respiratory therapist. During
529 the scan, the respiratory team had to ensure participants had a clear airway, requiring
530 monitoring of the participant's residual eye movements and physiological recordings (e.g., pulse
531 oximeter, EKG, and the ventilator, etc). Therefore, due to burden of longer functional scan times
532 in these participants, our recommended guidance for Stentrode deployment is to prioritize
533 maximizing coverage of M1, specifically the rostral wall of the central sulcus. To the extent that
534 the Stentrode BCI is larger than M1, it may be beneficial to bias the positioning more rostral so
535 as to be able to record activity from SMA as well, given its putative involvement in higher order
536 motor and cognitive processes that may be beneficial for complex BCI control^{43,44}. However,
537 while present device deployment may not warrant necessitating functional neuroimaging for
538 targeting, next-generation devices could be engineered to target smaller cortical vessels, where
539 a smaller cortical target is necessary. In these instances, functional neuroimaging protocols will
540 need to be improved to ensure a sufficient amount of functional data is acquired to guide
541 targeting of smaller cortical sites. More generally, for BCI devices with broad cortical coverage
542 (i.e., the Stentrode BCI, larger ECoG arrays), we recommend prioritizing anatomical targeting—
543 specifically M1—over individualized functional imaging, that is unless neuroimaging protocols
544 can be optimized (e.g., increased scan times and conditions) to yield sufficiently selective
545 activations without imposing undue risk or burden on participants with advanced disease.

546
547 There are several limitations with our investigation that are worth noting. First, we did not
548 perform any statistical corrections for the multiple comparisons, e.g., the 16 user-specific factors
549 tested ([Figure 5D-E](#)). The rationale for this decision was due to the highly exploratory nature of
550 the investigation. Our hope is that this data serves as a proof-of-concept to guide the design of
551 future studies with larger cohorts, as they become available. A second limitation is that our
552 estimation of the Stentrode BCI position was accurate solely along the coronal plane, but not
553 accurate in relation to the unique locations of individual electrodes within the SSS. Due to the
554 methodological difficulties with reliably extracting single electrode positions from the CT images
555 and computing distances for each electrode to various targets, we opted for a simpler estimation
556 that was accurate along the coronal axis and positioned within the center of the SSS
557 segmentation. A third limitation is that we provide a measure of motor BCI signal quality, not
558 BCI performance. Finally, considering the aim of the investigation was to pool data across 2
559 clinical trials (spanning over 5 years), there are differences in the referencing scheme of the
560 Stentrode BCI and the experimental design of the Motor Signal Test used to estimate Stentrode
561 BCI motor signal strength between the two study cohorts. Despite these differences, we did not
562 observe any differences in Stentrode BCI motor signal strength between participants from the
563 two trials, with a similar percentage of participants from each trial as high-responders (upper-
564 half of the sensitivity index distribution) and low-responders (lower-half of the sensitivity index
565 distribution; independent samples Mann-Whitney U test; $W=13.0$; $p=0.914$).

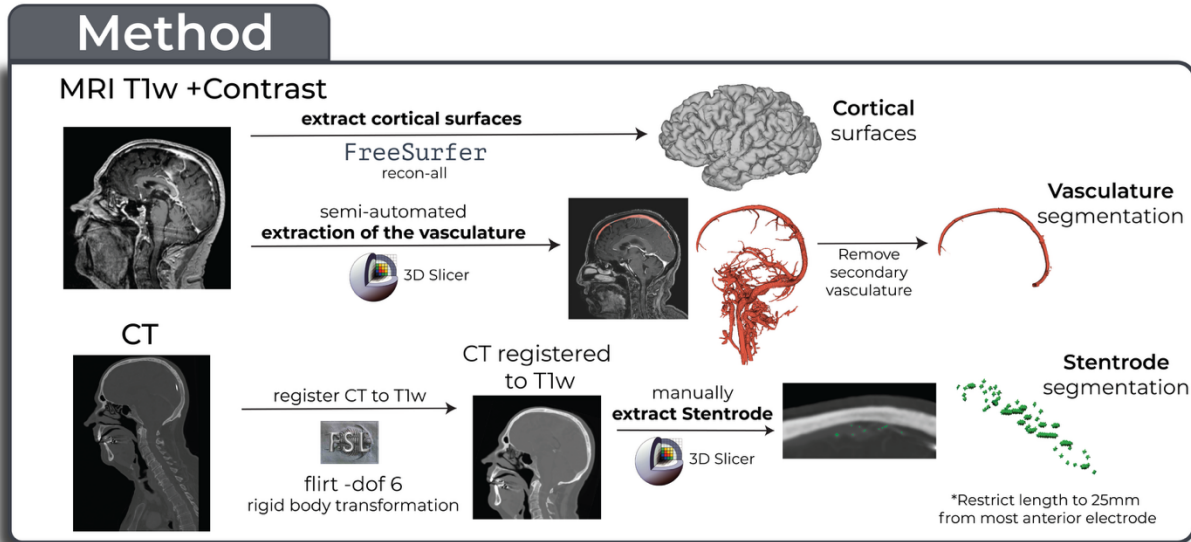
566
567 In conclusion, our study provides a comprehensive scientific framework for investigating how a
568 variety of user-specific factors contribute to recorded signal strength of implantable BCI
569 technologies. As more individuals are implanted with BCI devices, identifying key user-specific
570 predictors of BCI success will be essential for the long-term viability of the neurotechnology
571 industry. These predictors will be vital for refining patient selection, optimizing implant targeting
572 strategies and tailoring BCI hardware and software for specific clinical populations. By

573 identifying potential determinants of successful neural interfacing with the Stentrode BCI, we
574 hope this investigation offers some foundational insights into improving the clinical translation of
575 the Stentrode BCI and, more broadly, contribute to the advancement of all implantable BCI
576 technologies.

577 **Supplementary Results**
578

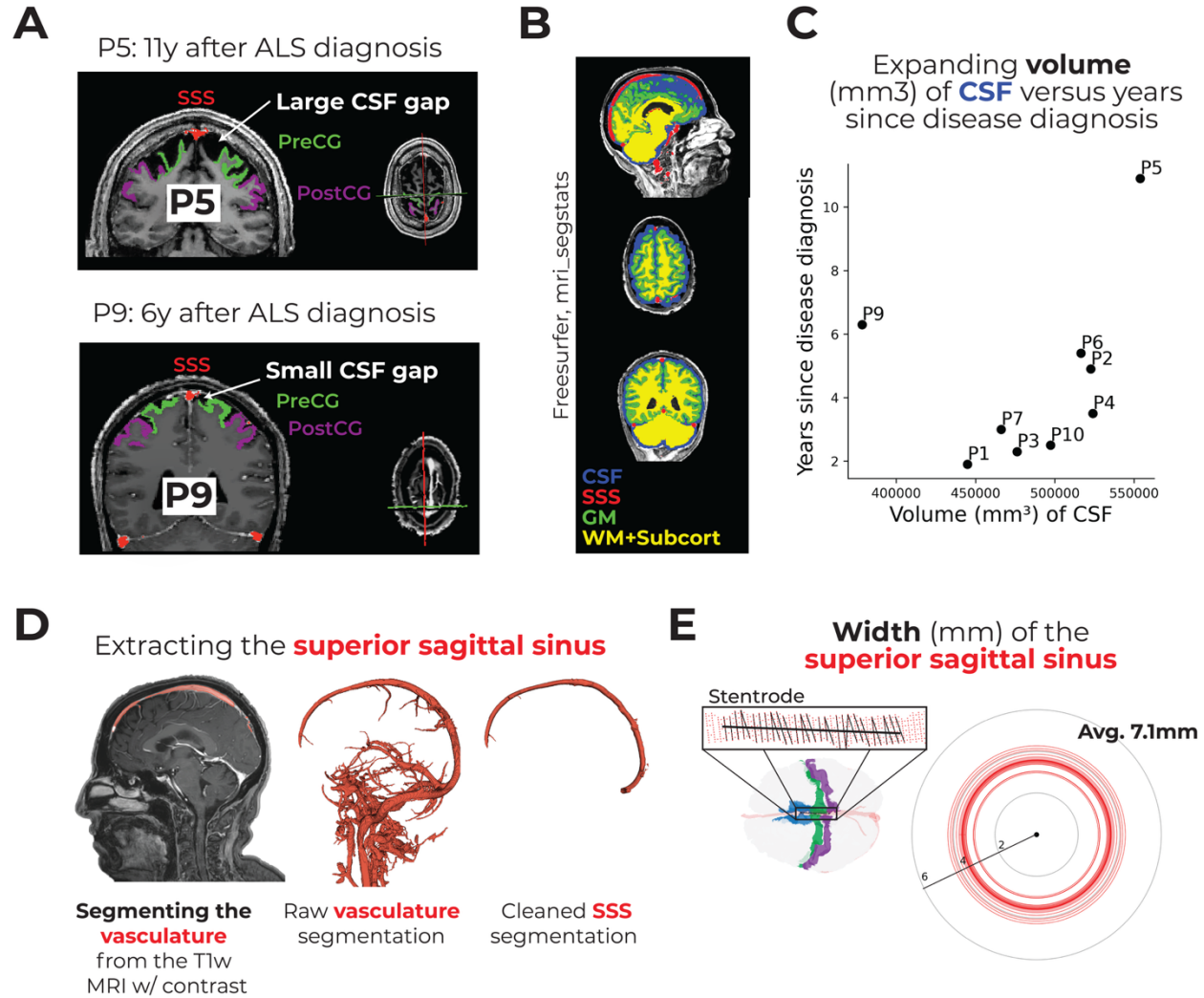


579 **Supp. Figure 1. Supplementary functional neuroimaging analyses.** (A) Number of
580 significant voxels (z -statistic > 2.3 ; z -threshold used in Figure 2) within the SMA (blue), M1
581 (green) and S1 (purple) regions. All participants can significantly activate a subset of voxels,
582 within all regions, during attempted movement. The data was visualized on a log-scale to
583 demonstrate that P5 significantly activated a subset of voxels. (B) Visualizing P5's functional
584 data at a lower minimum threshold (z -statistic > 1.96) within the precentral gyrus highlighted (in
585 blue) on both the inflated surfaces (top row) and pial surfaces (bottom row). (C) A subset of
586 participants underwent functional scans where bilateral hand movements were performed. The
587 bilateral ankle and bilateral hand activation maps are displayed. All other annotations are the
588 same as described in Figure 2.
589

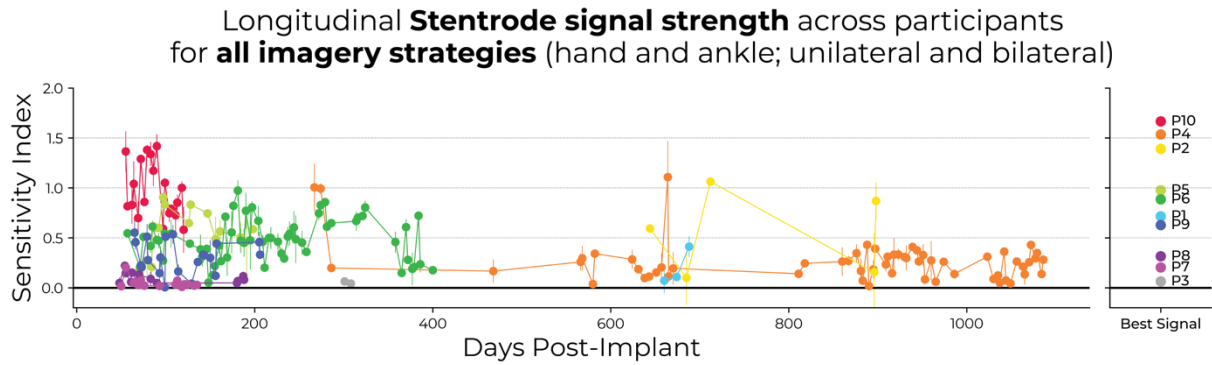


590
591
592
593

Supp. Figure 2. Method for generating a common coordinate space with the cortical surfaces, vasculature and Stentrode BCI. See the [Methods](#) for a detailed description of the method.

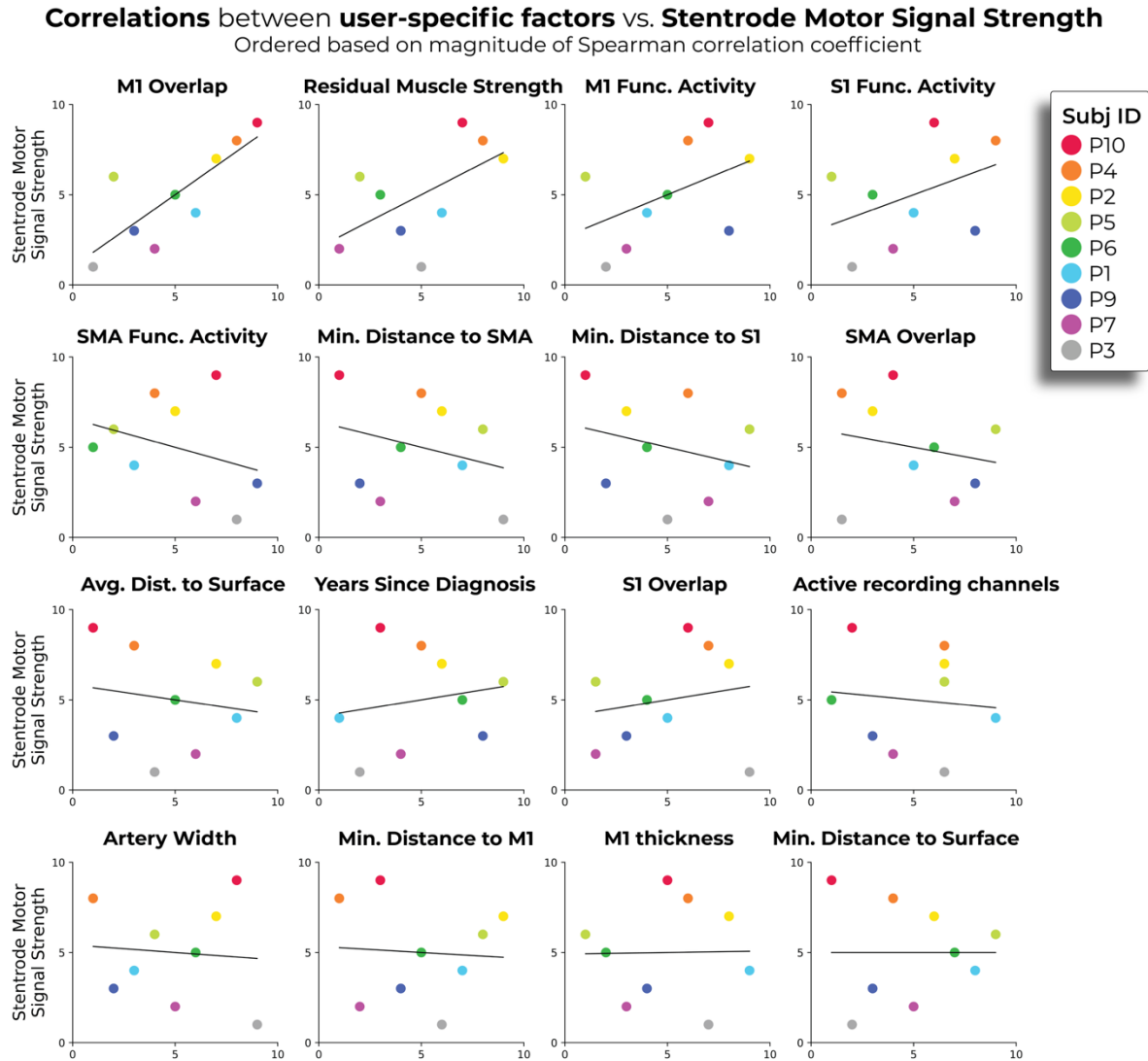


594
 595 **Supp. Figure 3. Segmenting the cerebrospinal fluid (CSF) and superior sagittal sinus (SSS) for Stentrode-implanted participants with adult-onset motor neuron diseases. (A)**
 596 *Visualizing the SSS, pre- and post-central gyri on the T1w + contrast MRI for the two*
 597 *participants with the most progressed ALS: P5 (top row) and P9 (bottom row). P5 shows an*
 598 *extensive gap, in this extreme slice example, between the SSS and the cortical surface filled*
 599 *with CSF. Alternatively, P9 generally shows a much more minimal gap. (B) To segment the*
 600 *CSF, we used freesurfer's mri_segstats function to generate segmentations of the CSF (blue),*
 601 *grey matter (GM; green), white matter and subcortical structures (both shown in yellow). As the*
 602 *CSF segmentation includes the SSS, we removed any SSS segmentation voxels from the CSF*
 603 *segmentation. We then computed a measure of whole-brain CSF volume (mm³) from the*
 604 *segmentation. (C) We observed a significant association between years since motor neuron*
 605 *disease diagnosis and total volume of CSF ($r_s=0.83$, $p=0.01$), though not when P9 was included*
 606 *($r_s=0.41$, $p=0.2$). (D) A visualization of one participant's segmentation of the neurovasculature*
 607 *overlaid on the T1w MRI, the raw vasculature segmentation in 3D space and the manually*
 608 *cleaned segmentation of the SSS. (E) Using the SSS segmentation, the diameter of the SSS*
 609 *was measured to be on average 7.1 ± 0.9 mm across Stentrode implanted participants.*
 610 *Individual red circles reflect the average SSS width for the points where the Stentrode is*
 611 *implanted.*
 612
 613



614
615 **Supp. Figure 4. Stentrode motor signal strength datasets for all imagery strategies.** While
616 the data plotted in [Figure 5C](#) is only for the preferred imagery strategy of each participant (either
617 hand or ankle), the data displayed here includes all imagery strategies.

It is made available under a [CC-BY 4.0 International license](https://creativecommons.org/licenses/by/4.0/).



618
619
620

Supp. Figure 5. Plotting correlations between all user-specific factors and Stentrode motor signal strength. All plotted data is the ranked values.

621 **Methods**

622

623 **Clinical trials and participant recruitment**

624 Study participants were involved in 1 of 2 clinical trials: SWITCH or COMMAND. The SWITCH
625 trial (n=4; participants P1 – P4; Clinicaltrials.gov: NCT03834857) was approved by the Human
626 Research Ethics Committees of St. Vincent’s Hospital, Royal Melbourne Hospital and Calvary
627 Health Care Bethlehem in Australia. The clinical protocol for this trial has been previously
628 published^{10,11}. The COMMAND early feasibility trial (n=6; participants P4 – P10;
629 Clinicaltrials.gov: NCT05035823) was conducted under an Investigational Device Exemption
630 from the U.S. Food and Drug Administration and approved by the Institutional Review Boards at
631 Western-Copernicus Group (1347924). Informed consent was obtained before any study
632 procedures were conducted and in accordance with the Declaration of Helsinki.

633

634 **Stentrode device and deployment**

635 The Stentrode (Synchron, USA) consists of 16 platinum electrodes, each with a 300 μm
636 diameter, mounted on a self-expanding nitinol scaffold measuring 8 × 40 mm. The inter-elctrode
637 spacing is approximately 3mm. The Stentrode is connected to a 50cm flexible endovascular
638 lead and inserted into an inductively powered internal telemetry unit¹¹ (ITU; Synchron, USA).
639 The device, surgical deployment procedure and signal acquisition have been previously
640 described in detail^{10,11}. In the SWITCH trial, a common reference channel was fixed to an
641 electrode located on the ITU. In the COMMAND trial, the reference channel was configurable
642 across one of the 16 channels or the electrode on the IRTU.

643

644 **Participants**

645 *Stentrode BCI group*

646 The Stentrode BCI group included ten participants [two females; mean age \pm STD = 58.4 \pm
647 12.6]. Eight participants were diagnosed with ALS, one participant diagnosed with PLS (P4),
648 and one participant diagnosed with an arterial ischemic stroke in the brainstem (P8; see [Table 1](#)
649 and [Supp. Table 1](#) for all participant demographics).

It is made available under a [CC-BY 4.0 International license](https://creativecommons.org/licenses/by/4.0/) .

Participant ID	P1	P2	P3	P4	P5	P6	P7	P8	P9	P10
Sex	M	M	M	M	M	M	M	F	F	M
Disease/injury	ALS	ALS	ALS	PLS	ALS	ALS	ALS	Pontine arterial ischemic stroke	ALS	Main-in-the-barrel ALS
Years since diagnosis, at time of consent	1.9y	4.9y	2.3y	3.5y	10.9y	5.4y	3.0y	13.5y	6.3y	2.5y
Mechanically ventilated, during study	N	N	N	N	Y	Y	Y	N	N	N
Preferred imagery strategy for Stentrode control	Left ankle	Both ankles	Right ankle	Both ankles	Both ankles	Right hand	Both ankles	Both ankles	Right hand	Right hand
Stentrode device version; # of connected (active) channels	V1;16	V1;15	V1;15	V1; 15	V2;15	V2;9	V2;13	V2;13	V2;12	V2;10

650 **Table 1. Participant demographics.** Regarding the host country of the clinical trial, the SWITCH
 651 trial was conducted in Australia (AUS) and the COMMAND EFS trial was conducted in the USA.
 652 Y=yes; N=no; PLS=primary lateral sclerosis; ALS=amyotrophic lateral sclerosis.

Participant ID	Baseline Functional Status
P1	Limited mobility of upper and lower body starting out, eventually developed pseudo-bulbar issues (e.g., intense coughing).
P2	Slow progressive condition; upper body started losing functionality and very slowly affected his lower limbs, causing him to be wheelchair bound. Breathing difficulties made it difficult for him to speak and made him tire easily.
P3	Fast progressing condition; affected his whole body.
P4	Slow progressing condition; limited movement of lower limb, but proficient upper limb movement. Had an injured right shoulder making him unable to raise hand above shoulder level.
P5	Locked in; mechanically ventilated via a tracheostomy to breathe, only able to slightly move left side of mouth to indicate 'no' and looks up to indicate 'yes'.
P6	Locked in; mechanically ventilated via a tracheostomy to breathe, only able to slightly smile and very slight movement of right index finger.
P7	Locked in; mechanically ventilated via a tracheostomy to breathe, no residual movement.
P8	Room air via a tracheostomy to breathe; can make noises with passy-muir valve; residual movement in left hand; looks up and down to indicate 'yes' and 'no'
P9	Used supplemental oxygen and a gastrostomy feeding tube; could blink and slightly smile; could make slight noises to indicate distress
P10	Man-in-the-barrel ALS; minimal control of upper limbs; ambulatory and verbal.

653 **Supplementary Table 1. Qualitative description of the functional status of participants.**

654

655 **Control group**

656 The control group included 16 participants [9 females; mean age \pm STD = 53.1 \pm 6.37; all right-
657 handed]. The only datasets analyzed from these participants were their structural T1w MRI
658 scans (acquired from a publically available dataset; see ref.²⁸ for additional information about
659 these participants, including MR scanning procedures). Importantly, there were no significant
660 differences between the Stentrode BCI group (with motor neuron diseases) and the control
661 group in age (Mann-Whitney independent samples test: $W=109.0$, $p=0.13$) or sex [though
662 trending; Chi-Squared test: $X_2(1)=3.3$, $p=0.06$].

663

664 **Manual muscle strength testing**

665 Prior to implantation, participants underwent manual muscle strength testing. This involved a
666 neurologist or physiatrist grading muscular contractions for different movements. For SWITCH
667 trial participants, the following movements were assessed: fingers, wrist, elbow, shoulder, hip,
668 knee, ankle, plantar flexion and dorsiflexion. For COMMAND trial participants, the following
669 movements were assessed: finger abduction (pinky), middle finger flexion, wrist extension,
670 elbow flexion, elbow extension, hip flexion, knee extension, ankle dorsiflexion, ankle plantar
671 flexion and big toe dorsiflexion. For all participants, movements were assessed separately for
672 the left and right sides of the body using the MRC muscle power scale^{16,17}, ranging from 0 to 5.
673 The scores reflect the following: 0 = no muscular contraction; 1 = visible muscle contraction, but
674 no movement at joint; 2 = movement at the joint, but not against gravity; 3 = movement against
675 gravity, but not against resistance; 4 = movement against resistance, but less than full; 5 =
676 movement against full resistance, normal strength. From this data, a bilateral whole-body
677 compound score was generated. Scores were averaged for each body-part across sides (left,
678 right) first and then averaged across body-parts, resulting in a measure of manual muscle
679 strength, which we refer to as residual muscle strength.

680

681 **Pre-implant MRI overview**

682 Prior to implantation, all participants underwent an MRI session which included structural and
683 functional imaging. Relevant for the present investigation, all participants underwent functional
684 motor mapping scans and a T1w structural scan with a contrast agent.

685

686 **Functional motor mapping**

687 To assess whether participants could activate cortical motor networks during attempted
688 movement, all participants underwent functional MRI scans while attempting to perform one or
689 more movements of individual body-parts including: right ankle, left ankle, both ankles or both
690 hands. For ankle movements, participants were instructed to repeatedly flex and extend their
691 ankles. For hand movements, participants were instructed to repeatedly open and close their
692 fingers. Importantly, the body-parts tested varied across participants, due to site-specific
693 modifications to the imaging protocol catered to each participant. To guide participants'
694 movements during scanning, instructions were delivered using audio- (i.e., Avotec MR-
695 compatible headphones) and/or text-cues, displayed via a visual display projected into the
696 scanner bore. The method for delivering cues (audio, text or both) varied across participants,
697 due to varying technical capacities at each scan site.

698
699 The functional task design was structured in a block-design, where each block consisted of a
700 15s OFF ("REST") period followed by a 15s ON ("MOVE") period. The number of block
701 repetitions varied between 8 – 10 across participants. The following participants performed 8
702 blocks: P1, P2, P3, P4, P6, P7, P10, followed by a 15s rest period. P8 performed 9 blocks
703 followed by a 15s rest period. P5 and P9 performed 10 blocks. Finally, the number of functional
704 runs varied from 1 – 4 depending on participants. For a detailed breakdown of the body-parts
705 and number of functional runs tested per participant, see [Supp. Table 2](#) below.

It is made available under a [CC-BY 4.0 International license](https://creativecommons.org/licenses/by/4.0/).

ID	MR Scanner; RF Coil; Site Location	Structural MRI (T1 MPRAGE)	Functional MRI (BOLD)	Body-parts tested (# of functional runs; # of motion outlier TRs > .9mm)
P1	<ul style="list-style-type: none"> 3T Siemens Prisma 32Ch Melbourne, AUS 	TR=1900ms TE=2.34ms TI=900ms FA=8° VoxelSize=0.9x0.9x1mm FOV=288x288mm Slices=208 Slice thickness=1.0mm	TR=2500ms TE=30ms Volumes=85 FA=90° VoxelSize=3.75x3.75mm FOV=64 x 64 mm Slices=34 Slice thickness=3.0mm	<ul style="list-style-type: none"> L ankle (1 run; 7) R ankle (1 run; 7)
P2	<ul style="list-style-type: none"> L ankle (1 run; 0) R ankle (1 run; 0)
P3	<ul style="list-style-type: none"> L ankle (1 run; 0) R ankle (1 run; 0)
P4	<ul style="list-style-type: none"> L ankle (1 run; 0) R ankle (1 run; 3)
P5	<ul style="list-style-type: none"> 3T GE SIGNA Architect 32Ch New York, USA 	TR=8412ms TE=3.168ms TI=1100ms FA=8° VoxelSize=1mm ³ FOV=256x256mm Slices= Slice thickness=1mm	TR=3000ms TE=60ms Volumes=100 FA=90° VoxelSize=3.75x3.75mm FOV=64x64mm Slices= Slice thickness=4.0mm	<ul style="list-style-type: none"> Both ankles (1 run; 0)
P6	<ul style="list-style-type: none"> 3T GE SIGNA Architect 32Ch New York, USA 	TR=8412ms TE=3.168ms TI=1100ms FA=8° VoxelSize=1mm ³ FOV=256x256mm Slices=194 Slice thickness=1mm	TR=3000ms TE=60ms Volumes=85 FA=90° VoxelSize=3.75x3.75mm FOV=64x64mm Slices=35 Slice thickness=4.0mm	<ul style="list-style-type: none"> L ankle (1 run; 1) R ankle (1 run; 2) Both ankles (2 runs; run1: 1; run2: 1) Both hands (4 runs; run1: 1; run2: 3; run3: 3; run4: 4)
P7	<ul style="list-style-type: none"> 3T Siemens Magnetom Biograph mMR 32Ch Pittsburgh, USA 	TR=1900ms TE=2.34ms TI=900ms FA=8° VoxelSize=0.9mm ³ FOV=256x256mm Slices=208 Slice thickness=0.9mm	TR=2500ms TE=30ms Volumes=85 FA=90° VoxelSize=2mm ³ FOV= 110x110mm Slices=32 Slice thickness=2.0mm	<ul style="list-style-type: none"> L ankle (1 run; 0) R ankle (1 run; 0)
P8	<ul style="list-style-type: none"> 3T Philips Igenia Elition X 32Ch Buffalo, USA 	TR=7599ms TE=3.4ms TI=900ms FA=8° VoxelSize=0.3x0.3mm FOV=240x240mm Slices=170 Slice thickness=1.0mm	TR=3000ms TE=35ms Volumes=95 FA=90° VoxelSize=1.79x1.79mm FOV=96x94mm Slices=36 Slice thickness=4.0mm	<ul style="list-style-type: none"> Both hands (1 run; 0) Both ankles (2 runs; run1: 6; run2: 9)
P9	<ul style="list-style-type: none"> 3T Philips Igenia Elition X 32Ch Buffalo, USA 	TR=7599ms TE=3.4ms TI=900ms FA=8° VoxelSize=0.3x0.3mm FOV=240x240mm Slices=170 Slice thickness=1.0mm	TR=3000ms TE=35ms Volumes=100 FA=90° VoxelSize=1.79x1.79mm FOV=96x94mm Slices=36 Slice thickness=4.0mm	<ul style="list-style-type: none"> Both hands (1 run; 6) Both ankles (2 runs; run1: 32; run2: 3)
P10	<ul style="list-style-type: none"> 3T Siemens Magnetom Biograph mMR 32Ch Pittsburgh, USA 	TR=1900ms TE=2.34ms TI=900ms FA=8° VoxelSize=0.9mm ³ FOV=256x256mm Slices=208 Slice thickness=0.9mm	TR=2500ms TE=30ms Volumes=85 FA=90° VoxelSize=2mm ³ FOV=110x110mm Slices=32 Slice thickness=2.0mm	<ul style="list-style-type: none"> L ankle (1 run; 0) R ankle (1 run; 0)

706 **Supplementary Table 2. MRI scanning information for participants.** L=left; R=right; FA=flip
 707 angle; FOV=field of view; TR=repetition time; TE=echo time; TI=inversion time; “...” = same as
 708 above.

709
710
711
712
713
714
715
716
717
718
719
720
721
722
723
724
725
726
727
728
729
730
731
732
733
734
735
736
737
738
739
740
741
742
743
744
745
746
747
748
749
750
751
752
753
754
755
756
757
758
759

MRI data acquisition

Participants were scanned at 1 of 4 MRI sites based in either: Melbourne (AUS), New York (USA), Buffalo (USA) or Pittsburgh (USA). As such, the scanner, head coil, structural- and functional MRI parameters vary across sites (for a breakdown, see [Supp. Table 2](#)). MRI images, for all participants, were obtained using a 3-Tesla scanner. Prior to running a structural MR scan, participants underwent a time-resolved angiography with interleaved stochastic trajectories (TWIST) scan whereby a multihance contrast agent was administered. Although the data from this sequence were not used in the current investigation, a subsequent structural anatomical scan was performed using a T1-weighted magnetization prepared rapid acquisition gradient echo sequence (MRPAGE) in the sagittal plane with residual contrast agent from the TWIST angiography. The structural scan sequence parameters vary across participants, described in detail in [Supp. Table 2](#). Next, functional data, based on the blood oxygenation level-dependent (BOLD) signal, were acquired using a gradient echo-planar imaging (EPI) sequence which included slices (32 or 34) with a slice thickness of either 2.0mm or 3.0mm, a repetition time (TR) of either 2500ms or 3000ms, and an echo time (TE) of 30ms. All other scan parameters are described in [Supp. Table 2](#). The motor fMRI scans had either 85, 95 or 100 volumes, depending on the participant (approximately 5 minutes).

fMRI analysis

Functional MRI data were processed by using FMRIB's Expert Analysis Tool (FEAT; Version 6.0), part of FSL (FMRIB's Software Library, www.fmrib.ox.ac.uk/fsl), in combination with custom bash, Python (version 3) and MATLAB scripts (R2019b, v9.7, The Mathworks Inc, Natick, MA). Cortical surface reconstructions were produced using FreeSurfer [v. 7.1.1^{45,46}] and Connectome Workbench (humanconnectome.org) software.

fMRI preprocessing

The following pre-statistical processing was applied: motion correction using MCFLIRT⁴⁷, non-brain removal using BET⁴⁸, spatial smoothing using a Gaussian kernel of FWHM 5mm for the functional task data, grand-mean intensity normalization of the entire 4D dataset by a single multiplicative factor, and high-pass temporal filtering (Gaussian-weighted least-squares straight line fitting, with $\sigma = 100$ s). Time-series statistical analysis was carried out using FILM with local autocorrelation correction⁴⁹. The time series model included trial onsets convolved with a double γ HRF function; six motion parameters were added as confound regressors. Indicator functions were added to model out single volumes identified to have excessive motion (>0.9 mm). A separate regressor was used for each high motion volume (deviating more than .9mm from the mean position). For the motor mapping scans, the median number of outlier volumes for an individual scan, across all participants, was 1 volume (range: 0 – 32).

Low level task-based analysis

We applied a general linear model (GLM) using FEAT to each functional run. Each movement's task data was modeled against rest resulting in z-statistic maps, where each voxel represents the statistical significance of functional activity relative to rest, with the results thresholded for significance. As previously described, the number of runs performed varied between 1 - 4 across participants, for a given task. For participants with just 1 run of a task, the resulting z-stats were registered to the participant's structural T1w image. For participants with multiple runs of a single task, estimates from the individual runs were averaged in a voxel-wise manner using a fixed effects model with a cluster forming z-threshold of 2.3 and a family-wise error corrected cluster significance threshold of $p < 0.05$. Run-averaged z-stats were registered to the participant's structural T1w scan using FLIRT.

760 **Cortical surface reconstruction**

761 Structural T1w images were used to reconstruct the pial and white-gray matter surfaces using
762 Freesurfer's recon-all command (<https://surfer.nmr.mgh.harvard.edu/fswiki/recon-all>). The grey
763 and white matter segmentations of the reconstructions were then visually inspected and
764 manually edited to correct any large geometric inaccuracies (for more information on the
765 method for performing manual corrections of cortical surface reconstructions, please
766 see https://surfer.nmr.mgh.harvard.edu/fswiki/FsTutorial/PialEdits_freeview). Surface co-
767 registration across hemispheres and participants was done using spherical alignment. Individual
768 surfaces were nonlinearly fitted to a template cortical surface, first in terms of the sulcal depth
769 map, and then in terms of the local curvature, resulting in an overlap of the fundus of the central
770 sulcus across participants⁵⁰.

771 **Mapping functional activity onto the cortical surface**

772 For surface-based analyses, functional mapping data, already registered to the structural T1w,
773 were then projected onto the cortical surface using the workbench command's *volume-to-*
774 *surface-mapping* function which included a ribbon-constrained mapping method. One important
775 consideration is that different tasks were attempted across participants. Therefore, for scans
776 where a single ankle was moved (right or left ankle), we opted to map the activity for only the
777 contralateral hemisphere, as displayed in [Figure 2](#). Alternatively, for scans involving moving
778 both ankles, activity for each hemisphere (where a single hemisphere activity would include
779 both the ipsi- and contra- activations) were mapped onto the cortical surface.

781 **Regions of interest**

782 Defined regions of interest (ROIs) were generated using one of two approaches: surface-to-
783 surface mapping of the Glasser Human Connectome Project parcellation atlas⁵¹ and (2) using
784 probabilistic cytoarchitectonic maps⁵⁰. From the Glasser atlas, the following regions were mapped
785 (using *mri_surf2surf*) onto each participant's cortical surface: M1 (BA4), S1 (BA3b) and medially
786 extended S1 (BA3b, BA5m, BA5mv, BA1). For the univariate ROI analysis, we were interested in
787 activity directly under the SSS. Therefore, we further restricted the left- and right-hemisphere M1
788 and S1 ROIs to their most medial portions. We also defined a SMA region, which does not have
789 strict anatomical boundaries⁵². Considering the Glasser atlas defines multiple sub-regions on the
790 medial surface, just rostral of M1 [the medial caudal portion of BA6, superior frontal language
791 area (SFL), and supplementary and cingulate eye field (SCEF)], we opted to use the SMA (pre-
792 SMA) region boundaries used in ref⁵³, defined using probabilistic cytoarchitectonic maps on the
793 group average cortical surface. These boundaries were then projected onto each participant's
794 cortical surface. Additionally, as some ROI analyses were performed on the volume, these ROIs
795 were mapped to the volume, using freesurfer's label-to-volume-mapping method with the ribbon-
796 constrained option.

797
798
799 As a supplementary analysis for P5, we generated the boundaries of the precentral gyrus using
800 the Desikan-Killiany Atlas (<https://surfer.nmr.mgh.harvard.edu/fswiki/CorticalParcellation>), default
801 to freesurfer. This was displayed in [Supp. Figure 1C](#).

802 **Univariate analyses**

803 *Visualizing activation maps*

804 As previously described, for each participant, statistically thresholded ankle activity were
805 mapped onto the cortical surface. In [Figure 2A](#), these activation maps were displayed with a
806 common minimum statistical threshold ($Z > 2.3$). As a supplementary analysis for 3 participants
807 that underwent additional scans when attempting to move their hands, we displayed the ankle
808 activation maps alongside the hand activation maps ([Supp. Figure 1C](#)). Next, we generated a
809 group-level ankle movement activation map, the individual participant activation maps (z-stats)
810

811 were averaged in a voxel-wise manner. This approach was taken, as opposed to using a mixed-
812 effects model, due to the task differences across participants. The resulting group average z-
813 stat was then mapped onto a standard cortical surface. This activity was minimally thresholded
814 ($Z > 2.3$) and displayed on a standard pial cortical surface (Figure 2B).

815

816 *Activity within regions of interest*

817 Using the SMA ROI and the medially constrained M1 and S1 ROIs, the average z-stat within
818 each region was extracted for each participant (Figure 2C). Additionally, to estimate the spatial
819 coverage of activity within the regions, the number of significantly activated voxels ($Z > 2.3$) was
820 computed (Supp. Figure 1B).

821

822 **Generating a superior sagittal sinus segmentation**

823 In the investigation, one feature we aimed to extract is spatial information about the SSS. To
824 generate this, we segmented out the neurovasculature in 3D Slicer (<https://www.slicer.org/>).
825 This was performed using a pipeline that leveraged a Vesselness filtering module,
826 comprehensively described at <https://github.com/lassoan/SlicerSegmentationRecipes>. The
827 resulting segmentation was then displayed on its own and edited manually to remove secondary
828 vessels. The resulting segmentation was then saved as a .STL file (see Supp. Figure 2).

829

830 **Determining the location of the Stentrode BCI**

831 *Using the post-implant CT image to isolate the Stentrode*

832 All participants underwent post-implant CT scans to determine the position of the Stentrode BCI.
833 CT scans were taken 3-months after implantation. Each participant's CT image was registered
834 to their structural T1w MRI scan using FSL's FLIRT (FMRIB's Linear Image Registration Tool).
835 To ensure the Stentrode image was not atypically morphed, a rigid-body registration was
836 performed (6 degrees of freedom) using the mutual information cost function. Finally, the search
837 range for the rotation parameters were set to $[-180^\circ, 180^\circ]$ along the x, y, and z axes. To extract
838 the location of the Stentrode, the CT-registered image was loaded into 3D Slicer. On a slice-by-
839 slice basis, the Stentrode was manually segmented out for each participant. The resulting
840 segmentation was saved as an .STL file (see Supp. Figure 2).

841

842 Next, we displayed the cortical surfaces and segmentations for the SSS and Stentrode in a
843 common coordinate space (see example in Figure 3A). First, we modified the length of the
844 manual Stentrode segmentation. Across participants, the resulting Stentrode segmentations
845 ranged in length from 26.7 – 33.4mm. However, the exact distance of the Stentrode's most
846 rostral electrode to the most caudal electrode is 25mm. Therefore, we restricted the length of
847 each segmentation from the most rostral point of the segmentation back 25mm. Next, we aimed
848 to generate a simplified approximation of the Stentrode position. We generated a straight line
849 from the most rostral point of the segmentation to the most caudal point of the segmentation.
850 We next wanted to curve this line and position it within the middle of the SSS. We used custom
851 code written in MATLAB, whereby the rostral and caudal line endpoints were positioned in the
852 center of their relative location in the SSS. The midpoint of the line was then similarly adjusted.
853 A polynomial fit was then applied to the line, generating a curved path that approximated the
854 Stentrode's real-world positioning within the SSS.

855

856 To generate the images in Figure 4 of the Stentrode BCI position with the cortical surfaces, a
857 spatially accurate Stentrode model (black) was then aligned to the segmentation such that the
858 most rostral segmentation point coincides with the most rostral point of the Stentrode model.
859 The Stentrode model was then manually positioned to best fit the orientation of the manual
860 segmentation.

861

862 **Computing spatial distances**

863 Using the 25mm curved Stentrode line, we defined a point along the line every 0.5mm. Then,
864 we computed the distance from each point to the nearest cortical surface vertex in the left
865 hemisphere and the right hemisphere (50 distance estimations per hemisphere). We displayed
866 a visualization of this approach in [Figure 3B](#). For each hemisphere separately, we computed 5
867 different distances: 1) the minimum distance of each of these projections to either the left or
868 right hemisphere (i.e., minimum distance to cortex), 2) the average distance to the cortical
869 surface, averaging across the lines for each hemisphere separately (i.e., average distance to
870 cortex), 3) the minimum distance to M1, 4) S1, and 5) SMA. We averaged the distances for
871 each hemisphere to get 1 value per participant. Finally, the width of the SSS was also
872 computed. This was performed by restricting the SSS segmentation to just what was in-line with
873 the Stentrode line and computing multiple distance estimations across the full extent of the SSS
874 segmentation (an example displayed in [Supp. Figure 3A](#)).

876 **Percent overlap of Stentrode and brain regions**

877 To compute a measure of overlap between the Stentrode and brain regions (SMA, M1, S1 etc.),
878 we defined the most rostral point of each region on the medial surface, for each hemisphere
879 separately. A 2-D coronal plane was generated at each point, such that it cut through the
880 Stentrode segmentation. Considering the brain regions are spatially continuous along the
881 medial wall, the boundaries of each region ran from the most rostral point of each region to the
882 most rostral point of the subsequent caudal region (e.g., SMA = rostral of SMA to rostral of M1).
883 The percent overlap values were computed by calculating the distance of Stentrode overlapping
884 each region and dividing these values by the total distance of the Stentrode (25mm). We
885 averaged the percent overlap values across hemispheres to get 1 value per region.

887 **Cortical thickness**

888 After the Glasser Atlas⁵¹ M1 and S1 boundaries were mapped to each participant's pial cortical
889 surfaces (using a ribbon-constrained manner), the masks were visualized on both the surface
890 and volume to ensure they were spatially accurate (i.e., only included the grey matter). To
891 compute cortical thickness, we implemented the *mri_segstats* command to compute the cortical
892 thickness for each region and hemisphere. We averaged the cortical thickness values across
893 hemispheres to get 1 value per region.

895 **Computing the volume of the cerebrospinal fluid**

896 To investigate whether the amount of CSF increases with cortical atrophy, we aimed to compute
897 a measure of CSF volume. We used FreeSurfer's *mri_segstats* tool to extract total volumes of
898 the CSF, grey matter, white matter and subcortical structures (visualized in [Supp. Figure 3B](#) for
899 1 participant). We then subtracted the SSS segmentation for each participant from the CSF
900 segmentation to yield an adjusted intracranial CSF estimate excluding the primary venous
901 structure.

903 **Computing a measure of Stentrode motor signal strength**

904 *Motor signal tests*

905 Throughout both clinical trials, participant engaged in a task to test their ability to generate a
906 click using their Stentrode BCI. The task involved refraining from making a click for 10s (rest
907 period) and attempting the corresponding movement on the screen within 10s (go period),
908 guided by visual cues. There were 10 trials per CCT run and every run finished with an
909 additional 10s rest period (for a breakdown of the number of sessions collected see [Supp. Table
910 3](#) below). All tests were conducted within the home of each participant.

Subj ID	Body-part tested (number of sessions)	Average number of blocks per session
P1	Left ankle (3)	2.33
P2	Both ankles (1), left ankle (4)	2.20
P3	Right ankle (2)	1
P4	Both ankles (58), left ankle (2)	2.25
P5	Both ankles (18)	2.44
P6	Both ankles (39), left hand (1), right hand (22)	2.38
P7	Both ankles (10), right ankle (1), both hands (1), right hand (3), right hip (1), mouth (2), left shoulder (1)	4.73
P8	Both ankles (13), left hand (1)	4.62
P9	Both ankles (4), right hand (20)	2.27
P10	Both ankles (1), right hand (19)	3.26

911 **Supp. Table 3. Number of Stentrode motor signal test sessions and body-parts tested**
 912 **across participants. The bolded body-part is the preferred body-part for Stentrode control.**
 913

914 *Sensitivity index*

915 The sensitivity index was calculated in the following steps. For each participant, channels with
 916 high impedance values (>700 kOhms) and exhibiting signs of erratic perturbations via visual
 917 inspection were omitted. Data from the remaining channels were bandpass filtered at 100-200
 918 Hz with a 3rd order Butterworth infinite impulse response filter, based on a previous study
 919 showing that movement-related modulation in Stentrode recordings is most prominent within
 920 this frequency range¹⁴. Instantaneous power within 100ms non-overlapping windows were
 921 derived by calculating the log of the variance per channel, then the values were averaged
 922 across the channels. The sensitivity index (d') was calculated between all rest periods and go
 923 periods, where:

924
$$d' = 2 \frac{\mu_{go\ period} - \mu_{rest\ period}}{\sigma_{go\ period} + \sigma_{rest\ period}}$$

925
 926 And μ and σ denote the mean and the standard deviation of each period. For each participant,
 927 their highest sensitivity index value was then used as their Stentrode motor signal strength
 928 value.
 929

930 **Statistical analyses**

931 All statistical analyses were performed using either Python scripts utilizing `scipy.stats` and
 932 `statsmodels.stats.multitest` or JASP (0.17.2.1). Tests for normality were conducted using a
 933 Shapiro–Wilk test. Though, due to the small number of samples ($n=10$), we opted to primarily
 934 use non-parametric statistics in most instances. For the functional neuroimaging data, when
 935 comparing whether 1 region had more activity than another region, we used a paired Wilcoxon-
 936 signed rank test. For the structural neuroimaging data, when comparing cortical thickness
 937 measures between regions (M1, S1) and groups (motor neuron disease, controls), we used a
 938 repeated measures ANOVA with region as a within-subject factor and group as the between-
 939 subject factor. Post-hoc group comparisons were performed with non-parametric Mann Whitney
 940 U Tests where p-values were corrected for 2 comparisons. Additionally, when comparing
 941 demographics between the Stentrode participants with motor neuron diseases and the control
 942 participants, a Mann Whitney U-test was used to test for differences in age and a chi-squared
 943 test was used to test for differences in sex. For the Stentrode motor signal strength data, for
 944 each participant, we tested whether values were significantly greater than 0 using a Wilcoxon
 945 signed-rank test with 0 set as the test value. For the correlation analyses, we used non-
 946 parametric Spearman correlations. Finally, to investigate the relationship between selected

947 predictors and motor signal strength (sensitivity index), we performed a Lasso regression
948 analysis. To standardize the data, we applied a standard scaling procedure to the predictor
949 variables. The Lasso model was fitted with an alpha value of 0.1, which is a regularization
950 parameter that controls the strength of the penalty on the coefficients. A threshold of 0.05 was
951 used for statistical significance.
952

953 **Acknowledgements:** We thank our study participants for their immense generosity and
954 dedication to contributing to this research. We thank Prof. Tamar Makin for sharing the control
955 participant dataset. Finally, we thank Dr. Grace Edwards and Prof. Jessica Taubert for feedback
956 on imaging analyses. For participants P7 and P10, the imaging scans were conducted at the
957 University of Pittsburgh's Magnetic Resonance Research Center (RRID:SCR_025215).
958

959 **Conflict of interest:** P.Y. and T.O. are employees at *Synchron Inc.* and hold stock options.
960 T.O. is one of the founding directors and shareholders of Synchron Inc. T.O. has a patent for the
961 Stentrode (US 10485968 B2). D.W. is a cofounder and shareholder of ReachNeuro and holds
962 stock options from NeuroOne and NeuronOff. H.R.S., D.L., S.M., D.P., R.N., N.H., and J.C.,
963 have no conflict of interests to report.
964

965 **Funding:** Research reported in this publication was supported by the National Institute Of
966 Neurological Disorders And Stroke of the National Institutes of Health under Award Number
967 UH3NS120191 for the COMMAND trial and was funded by Synchron for the SWITCH trial. The
968 content is solely the responsibility of the authors and does not necessarily represent the official
969 views of the National Institutes of Health. H.R.S was supported by a research fellowship from
970 the National Institute of Mental Health of the National Institutes of Health (F32MH139145).
971

972 **Data availability statement:** The data cannot be made publicly available upon publication
973 because they contain commercially sensitive information. The data that supports the primary
974 findings of this study are available upon reasonable request.
975

976 **Authors contributions:** HRS, PY, DJW and JLC conceived the investigation. DJW, DFP, and
977 TJO secured funding. NYH, DFP and DL coordinated clinical management. CHM and FL
978 supported MRI scanning at one of the scan sites. RGN, EL and SM performed the implantation
979 surgeries at one of the sites. HRS led the data analysis with assistance from PY and CH while
980 supervised by JLC. HRS and JLC wrote the paper and all authors (HRS, PY, AF, NC, AS, CH,
981 FL, CHM, KH, SM, NYH, RGN, EL, DFP, DL, TJO, DJW, JLC) critically revised the text and
982 approved the final version.

983 **References**

- 984
- 985 1. Rapeaux, A. B. & Constandinou, T. G. Implantable brain machine interfaces: first-in-human studies,
- 986 technology challenges and trends. *Current Opinion in Biotechnology* **72**, 102–111 (2021).
- 987 2. Sawyer, A. *et al.* Meeting the Needs of People With Severe Quadriplegia in the 21st Century: The
- 988 Case for Implanted Brain–Computer Interfaces. *Neurorehabil Neural Repair* **38**, 877–886 (2024).
- 989 3. Abiri, R., Borhani, S., Sellers, E. W., Jiang, Y. & Zhao, X. A comprehensive review of EEG-based
- 990 brain–computer interface paradigms. *J. Neural Eng.* **16**, 011001 (2019).
- 991 4. Kozai, T. D. Y., Jaquins-Gerstl, A. S., Vazquez, A. L., Michael, A. C. & Cui, X. T. Brain Tissue
- 992 Responses to Neural Implants Impact Signal Sensitivity and Intervention Strategies. *ACS Chem.*
- 993 *Neurosci.* **6**, 48–67 (2015).
- 994 5. Woeppel, K. *et al.* Explant Analysis of Utah Electrode Arrays Implanted in Human Cortex for Brain-
- 995 Computer-Interfaces. *Front Bioeng Biotechnol* **9**, 759711 (2021).
- 996 6. Bjånes, D. A. *et al.* Quantifying physical degradation alongside recording and stimulation
- 997 performance of 980 intracortical microelectrodes chronically implanted in three humans for 956-2246
- 998 days. *Acta Biomaterialia* (2025) doi:10.1016/j.actbio.2025.02.030.
- 999 7. Degenhart, A. D. *et al.* Histological Evaluation of a Chronically-implanted Electrocorticographic
- 1000 Electrode Grid in a Non-human Primate. *J Neural Eng* **13**, 046019 (2016).
- 1001 8. Sponheim, C. *et al.* Longevity and reliability of chronic unit recordings using the Utah, intracortical
- 1002 multi-electrode arrays. *J. Neural Eng.* **18**, 066044 (2021).
- 1003 9. Patrick-Krueger, K. M., Burkhart, I. & Contreras-Vidal, J. L. The state of clinical trials of implantable
- 1004 brain–computer interfaces. *Nat Rev Bioeng* **3**, 50–67 (2025).
- 1005 10. Mitchell, P. *et al.* Assessment of Safety of a Fully Implanted Endovascular Brain–Computer Interface
- 1006 for Severe Paralysis in 4 Patients: The Stentrod With Thought-Controlled Digital Switch (SWITCH)
- 1007 Study. *JAMA Neurology* **80**, 270–278 (2023).
- 1008 11. Oxley, T. J. *et al.* Motor neuroprosthesis implanted with neurointerventional surgery improves
- 1009 capacity for activities of daily living tasks in severe paralysis: first in-human experience. *Journal of*
- 1010 *NeuroInterventional Surgery* **13**, 102–108 (2021).

- 1011 12. Kunigk, N. G. *et al.* Motor somatotopy impacts imagery strategy success in human intracortical brain–
1012 computer interfaces. *J. Neural Eng.* **22**, 026004 (2025).
- 1013 13. Jude, J. J. *et al.* An intuitive, bimanual, high-throughput QWERTY touch typing neuroprosthesis for
1014 people with tetraplegia. 2025.04.01.25324990 Preprint at
1015 <https://doi.org/10.1101/2025.04.01.25324990> (2025).
- 1016 14. Kacker, K. *et al.* Motor activity in gamma and high gamma bands recorded with a Stentrode from the
1017 human motor cortex in two people with ALS. *J. Neural Eng.* **22**, 026036 (2025).
- 1018 15. Hahn, N. V. *et al.* Long-term performance of intracortical microelectrode arrays in 14 BrainGate
1019 clinical trial participants. 2025.07.02.25330310 Preprint at
1020 <https://doi.org/10.1101/2025.07.02.25330310> (2025).
- 1021 16. Kendall, P., McCreary, E. K., Provance, P. G., Rodgers, M. M. & Romani, W. A. *Muscles Testing and*
1022 *Function with Posture and Pain*. (Lippincott Williams & Wilkins, Baltimore, MD, 2005).
- 1023 17. Paternostro-Sluga, T. *et al.* Reliability and validity of the Medical Research Council (MRC) scale and
1024 a modified scale for testing muscle strength in patients with radial palsy. *J Rehabil Med* **40**, 665–671
1025 (2008).
- 1026 18. Akselrod, M. *et al.* Anatomical and functional properties of the foot and leg representation in areas
1027 3b, 1 and 2 of primary somatosensory cortex in humans: A 7T fMRI study. *NeuroImage* **159**, 473–487
1028 (2017).
- 1029 19. Northall, A. *et al.* Multimodal layer modelling reveals in vivo pathology in amyotrophic lateral
1030 sclerosis. *Brain* **147**, 1087–1099 (2024).
- 1031 20. Braak, H. *et al.* Amyotrophic lateral sclerosis—a model of corticofugal axonal spread. *Nat Rev Neurol*
1032 **9**, 708–714 (2013).
- 1033 21. Mezzapesa, D. M. *et al.* Cortical Thinning and Clinical Heterogeneity in Amyotrophic Lateral
1034 Sclerosis. *PLoS One* **8**, e80748 (2013).
- 1035 22. Agosta, F. *et al.* The Cortical Signature of Amyotrophic Lateral Sclerosis. *PLOS ONE* **7**, e42816
1036 (2012).

- 1037 23. Kwan, J. Y., Meoded, A., Danielian, L. E., Wu, T. & Floeter, M. K. Structural imaging differences and
1038 longitudinal changes in primary lateral sclerosis and amyotrophic lateral sclerosis. *NeuroImage:*
1039 *Clinical* **2**, 151–160 (2013).
- 1040 24. Roccatagliata, L., Bonzano, L., Mancardi, G., Canepa, C. & Caponnetto, C. Detection of motor cortex
1041 thinning and corticospinal tract involvement by quantitative MRI in amyotrophic lateral sclerosis.
1042 *Amyotroph Lateral Scler* **10**, 47–52 (2009).
- 1043 25. Verstraete, E. *et al.* Structural MRI reveals cortical thinning in amyotrophic lateral sclerosis. *J Neurol*
1044 *Neurosurg Psychiatry* **83**, 383–388 (2012).
- 1045 26. Schuster, C. *et al.* Cortical thinning and its relation to cognition in amyotrophic lateral sclerosis.
1046 *Neurobiology of Aging* **35**, 240–246 (2014).
- 1047 27. Walhout, R. *et al.* Cortical thickness in ALS: towards a marker for upper motor neuron involvement. *J*
1048 *Neurol Neurosurg Psychiatry* **86**, 288–294 (2015).
- 1049 28. Schone, H. R. *et al.* Stable cortical body maps before and after arm amputation. *Nat Neurosci* 1–7
1050 (2025) doi:10.1038/s41593-025-02037-7.
- 1051 29. Norris, F. *et al.* Onset, natural history and outcome in idiopathic adult motor neuron disease. *Journal*
1052 *of the Neurological Sciences* **118**, 48–55 (1993).
- 1053 30. Hammer, R. P., Tomiyasu, U. & Scheibel, A. B. Degeneration of the human Betz cell due to
1054 amyotrophic lateral sclerosis. *Experimental Neurology* **63**, 336–346 (1979).
- 1055 31. Appel, S. H., Beers, D., Siklos, L., Engelhardt, J. I. & Mosier, D. R. Calcium: the Darth Vader of ALS.
1056 *Amyotroph Lateral Scler Other Motor Neuron Disord* **2 Suppl 1**, S47-54 (2001).
- 1057 32. Vansteensel, M. J. *et al.* Longevity of a Brain–Computer Interface for Amyotrophic Lateral Sclerosis.
1058 *New England Journal of Medicine* **391**, 619–626 (2024).
- 1059 33. Baumann, S. B., Wozny, D. R., Kelly, S. K. & Meno, F. M. The electrical conductivity of human
1060 cerebrospinal fluid at body temperature. *IEEE Transactions on Biomedical Engineering* **44**, 220–223
1061 (1997).
- 1062 34. Vansteensel, M. J. *et al.* Fully Implanted Brain–Computer Interface in a Locked-In Patient with ALS.
1063 *New England Journal of Medicine* **375**, 2060–2066 (2016).

- 1064 35. Card, N. S. *et al.* An Accurate and Rapidly Calibrating Speech Neuroprosthesis. *New England*
1065 *Journal of Medicine* **391**, 609–618 (2024).
- 1066 36. Willett, F. R. *et al.* A high-performance speech neuroprosthesis. *Nature* **620**, 1031–1036 (2023).
- 1067 37. Angrick, M. *et al.* Online speech synthesis using a chronically implanted brain–computer interface in
1068 an individual with ALS. *Sci Rep* **14**, 9617 (2024).
- 1069 38. Proudfoot, M., Bede, P. & Turner, M. R. Imaging Cerebral Activity in Amyotrophic Lateral Sclerosis.
1070 *Front Neurol* **9**, 1148 (2019).
- 1071 39. Knudsen, L. *et al.* Laminar fMRI in the locked-in stage of amyotrophic lateral sclerosis shows
1072 preserved activity in layer Vb of primary motor cortex. *Aperture Neuro* **4**, (2024).
- 1073 40. Maekawa, S. *et al.* Cortical selective vulnerability in motor neuron disease: a morphometric study.
1074 *Brain* **127**, 1237–1251 (2004).
- 1075 41. Toft, M. H., Gredal, O. & Pakkenberg, B. The size distribution of neurons in the motor cortex in
1076 amyotrophic lateral sclerosis. *J Anat* **207**, 399–407 (2005).
- 1077 42. Gredal, O., Pakkenberg, H., Karlsborg, M. & Pakkenberg, B. Unchanged total number of neurons in
1078 motor cortex and neocortex in amyotrophic lateral sclerosis: a stereological study. *Journal of*
1079 *Neuroscience Methods* **95**, 171–176 (2000).
- 1080 43. Tanji, J. & Mushiake, H. Comparison of neuronal activity in the supplementary motor area and
1081 primary motor cortex. *Brain Res Cogn Brain Res* **3**, 143–150 (1996).
- 1082 44. Lara, A. H., Cunningham, J. P. & Churchland, M. M. Different population dynamics in the
1083 supplementary motor area and motor cortex during reaching. *Nat Commun* **9**, 2754 (2018).
- 1084 45. Dale, A. M., Fischl, B. & Sereno, M. I. Cortical surface-based analysis. I. Segmentation and surface
1085 reconstruction. *Neuroimage* **9**, 179–194 (1999).
- 1086 46. Fischl, B., Liu, A. & Dale, A. M. Automated manifold surgery: constructing geometrically accurate and
1087 topologically correct models of the human cerebral cortex. *IEEE Trans Med Imaging* **20**, 70–80
1088 (2001).
- 1089 47. Jenkinson, M., Bannister, P., Brady, M. & Smith, S. Improved Optimization for the Robust and
1090 Accurate Linear Registration and Motion Correction of Brain Images. *NeuroImage* **17**, 825–841
1091 (2002).

- 1092 48. Smith, S. M. Fast robust automated brain extraction. *Human Brain Mapping* **17**, 143–155 (2002).
- 1093 49. Woolrich, M. W., Ripley, B. D., Brady, M. & Smith, S. M. Temporal Autocorrelation in Univariate
1094 Linear Modeling of fMRI Data. *NeuroImage* **14**, 1370–1386 (2001).
- 1095 50. Fischl, B. *et al.* Cortical folding patterns and predicting cytoarchitecture. *Cereb Cortex* **18**, 1973–1980
1096 (2008).
- 1097 51. Glasser, M. F. *et al.* A multi-modal parcellation of human cerebral cortex. *Nature* **536**, 171–178
1098 (2016).
- 1099 52. Nachev, P., Kennard, C. & Husain, M. Functional role of the supplementary and pre-supplementary
1100 motor areas. *Nat Rev Neurosci* **9**, 856–869 (2008).
- 1101 53. Wiestler, T. & Diedrichsen, J. Skill learning strengthens cortical representations of motor sequences.
1102 *eLife* **2**, e00801 (2013).
- 1103